Analytical Integrate-and-Fire Neuron Models with Conductance-Based Dynamics for Event-Driven Simulation Strategies

Michelle Rudolph
Rudolph@iaf.cnrs-gif.fr
Alain Destexhe
Alain.Destexhe@iaf.cnrs-gif.fr
Unité de Neuroscience Intégratives et Computationnelles, CNRS,
91198 Gif-sur-Yvette, France

Event-driven simulation strategies were proposed recently to simulate integrate-and-fire (IF) type neuronal models. These strategies can lead to computationally efficient algorithms for simulating large-scale networks of neurons; most important, such approaches are more precise than traditional clock-driven numerical integration approaches because the timing of spikes is treated exactly. The drawback of such event-driven methods is that in order to be efficient, the membrane equations must be solvable analytically, or at least provide simple analytic approximations for the state variables describing the system. This requirement prevents, in general, the use of conductance-based synaptic interactions within the framework of event-driven simulations and, thus, the investigation of network paradigms where synaptic conductances are important. We propose here a number of extensions of the classical leaky IF neuron model involving approximations of the membrane equation with conductance-based synaptic current, which lead to simple analytic expressions for the membrane state, and therefore can be used in the event-driven framework. These conductance-based IF (gIF) models are compared to commonly used models, such as the leaky IF model or biophysical models in which conductances are explicitly integrated. All models are compared with respect to various spiking response properties in the presence of synaptic activity, such as the spontaneous discharge statistics, the temporal precision in resolving synaptic inputs, and gain modulation under in vivo–like synaptic bombardment. Being based on the passive membrane equation with fixed-threshold spike generation, the proposed gIF models are situated in between leaky IF and biophysical models but are much closer to the latter with respect to their dynamic behavior and response characteristics, while still being nearly as computationally efficient as simple IF neuron models. gIF models should therefore provide a useful tool for efficient and precise simulation of large-scale neuronal networks with realistic, conductance-based synaptic interactions.

1 Introduction

Computational modeling approaches face a problem linked to the size of neuronal populations necessary to describe phenomena that are relevant at macroscopic biological scales, for example, at the level of the neocortex or visual cortex. Tens to hundreds of thousands of neurons, each synaptically linked with tens of thousands of others, organized in computational "modules" (e.g., Mountcastle, 1997), might be necessary to capture emergent functional properties and realistic dynamic behaviors. However, simulations of such modules are still beyond the limits of currently available conventional computational hardware if the neuronal units, as building blocks of the network module, are endowed with biophysically realistic functional dynamics. In such a case, the only reasonable compromise is to trade off complex dynamics in neuronal units with the achievable scale of the simulated network module. Indeed, reducing the neuronal dynamics down to that of simple integrate-and-fire (IF) neurons allows the efficient modeling of networks with tens to hundreds of thousands of sparsely interconnected neurons (e.g., Brunel, 2000; Wielaard, Shelley, McLaughlin, & Shapley, 2001; Shelley, McLaughlin, Shapley, & Wielaard, 2002; Delorme & Thorpe, 2003; Mehring, Hehl, Kubo, Diesmann, & Aertsen, 2003; Hill & Tononi, 2005).

Another way for optimizing neural network simulations is to search for more efficient modeling strategies. In biophysical models, neuronal dynamics is described by systems of coupled differential equations. Such systems are in general not analytically solvable, and numerical methods based on a discretization of space and time remain the principal simulation tool. A variety of techniques exist, which all have in common that the state variables of the system in question are evaluated for specific points of a discretized time axis. In such *synchronous* or *clock-driven* approaches, the algorithmic complexity and, hence, computational load scale linearly with the chosen temporal resolution. The latter introduces an artificial cutoff for timescales captured by the simulation and in this way sets strict limits for describing short-term dynamical transients (Tsodyks, Mit'kov, & Sompolinsky, 1993; Hansel, Mato, Meurier, & Neltner, 1998) and might have a crucial impact on the accuracy of simulations with spike-timing depending plasticity (STDP) or dynamic synapses (e.g., Markram, Wang, & Tsodyks, 1998; Senn, Markram, & Tsodyks, 2000).

Recently, a new and efficient approach was proposed (Watts, 1994; Mattia & Del Giudice, 2000; Reutimann, Giugliano, & Fusi, 2003) that sets the algorithmic complexity free from its dependence on the temporal resolution and, thus, from the constraints imposed on timescales of involved biophysical processes. In such *asynchronous* or *event-driven* approaches, the gain in accuracy is counterbalanced by the fact that the computational load scales linearly with the number of events, that is, with the average activity,

in the network. The latter strongly constrains the dynamic regimes which can be simulated efficiently. However, a coarse evaluation of this activity-dependent computational load suggests that the event-driven simulation strategy remains an efficient and more exact alternative to clock-driven approaches if cortical activity typically seen in vivo is considered (for a review, see Destexhe, Rudolph, & Paré, 2003).

The event-driven approach was successfully applied in a variety of contexts. These range from networks of spiking neurons with complex dynamics and focused on hardware implementations (Watts, 1994; Giugliano, 2000; Mattia & Del Giudice, 2000), up to networks of several hundreds of thousands of neurons modeling the processing of information in the visual cortex (Delorme, Gautrais, van Rullen, & Thorpe, 1999; Delorme & Thorpe, 2003). Recently, stochastic neuronal dynamics was made accessible to the event-based approach based on the analytic expression of the probability density function for the evolution of the state variable (Reutimann et al., 2003). This approach is applicable in cases in which neuronal dynamics can be described by stochastic processes, such as intrinsically noisy neurons or neurons with synaptic noise stemming from their embedding into larger networks. The latter provides an efficient simulation strategy for studying networks of interacting neurons with an arbitrary number of external afferents, modeled in terms of effective stochastic processes (Ricciardi & Sacerdote, 1979; Lánský & Rospars, 1995; Destexhe, Rudolph, Fellous, & Sejnowski, 2001).

So far, concrete applications of event-driven strategies of IF dynamics have been restricted to current-based synaptic interactions (Mattia & Del Giudice, 2000; Reutimann et al., 2003; Hines & Carnevale, 2004). However, to simulate states of intense activity similar to cortical activity in vivo, in particular high-conductance states with rapid synaptically driven transient changes in the membrane conductance (Destexhe et al., 2003), it is necessary to consider conductance-based synaptic interactions. In this letter, we propose an extension of the classical leaky IF neuron model (Lapicque, 1907; Knight 1972), the gIF model, which incorporates various aspects of presynaptic activity dependent state dynamics seen in real cortical neurons in vivo. The relative simplicity of this extension provides analytic expressions for the state variables, which allow this model to be used together with event-driven simulation strategies. This therefore provides the basis for efficient and exact simulations of large-scale networks with realistic synaptic interactions. In the first half of this letter, we outline the basic idea and introduce three analytic extensions of the classic leaky IF neuron model that incorporate presynaptic-activity dependent state dynamics as well as the state-dependent scaling of synaptic inputs. The second half of the letter is dedicated to a detailed investigation of the dynamics of these different models, specifically in comparison with more realistic biophysical models of cortical neurons as well as the widely used leaky IF neuron model.

2 Integrate-and-Fire Neuron Models with Presynaptic-Activity Dependent State Dynamics

After a brief review of the leaky integrate-and-fire (LIF) neuron model, the core idea behind the incorporation of specific aspects of presynaptic-activity dependent state dynamics is presented. Based on this, three extended integrate-and-fire models of increasing complexity but with simple analytic forms of their state variables are proposed.

2.1 The Classic LIF Neuron Model. In the simplest form of IF neuron models, the leaky integrate-and-fire model (Lapicque, 1907; Knight, 1972), the evolution of the state variable is described by the following first-order differential equation,

$$\tau_m \frac{dm(t)}{dt} + m(t) = 0, \tag{2.1}$$

where τ_m denotes the membrane time constant and $m(t)$ the state variable $m_{rest} \leq m(t) \leq m_{thres}$ at time t. Upon arrival of a synaptic input at time t_0, $m(t)$ is instantaneously updated by Δm, that is, $m(t_0) \longrightarrow m(t_0) + \Delta m$. After that, the state variable decays exponentially with time constant τ_m toward a resting state m_{rest} (for the moment, we assume $m_{rest} = 0$) until the arrival of a new synaptic input at time t_1 (see Figure 1A, cLIF). If $m(t)$ crosses a threshold value m_{thres} (usually assumed to be $m_{thres} = 1$), the cell fires a spike and is reset to its resting value m_{rest}, at which it stays for an absolute refractory period t_{ref}. The simple form of equation 2.1 allows an explicit solution in between the arrival of synaptic events, given by

$$m(t) = m(t_0)\, e^{-\frac{t-t_0}{\tau_m}}, \tag{2.2}$$

where $t_0 \leq t < t_1$ and $0 \leq m(t) \leq 1$.

Depending on the value of the membrane time constant τ_m, we will distinguish two different LIF models. First, a model with large τ_m, of the order of membrane time constants typically observed in low-conductance states, will be referred to as a classic leaky integrate-and-fire (cLIF) neuron model. Second, a LIF model with small τ_m mimicking a (static) high-conductance state will be referred to as a very leaky integrate-and-fire (vLIF) neuron model.

2.2 LIF Neuron Models with Presynaptic-Activity Dependent State Dynamics. In real neurons, the effect of synaptic inputs can be described by transient changes in the conductance of the postsynaptic membrane. This synaptic conductance component $G_s(t)$ adds to a constant leak conductance G_L (the contribution of active membrane conductances will not be

considered here for simplicity), yielding a time-dependent total membrane conductance,

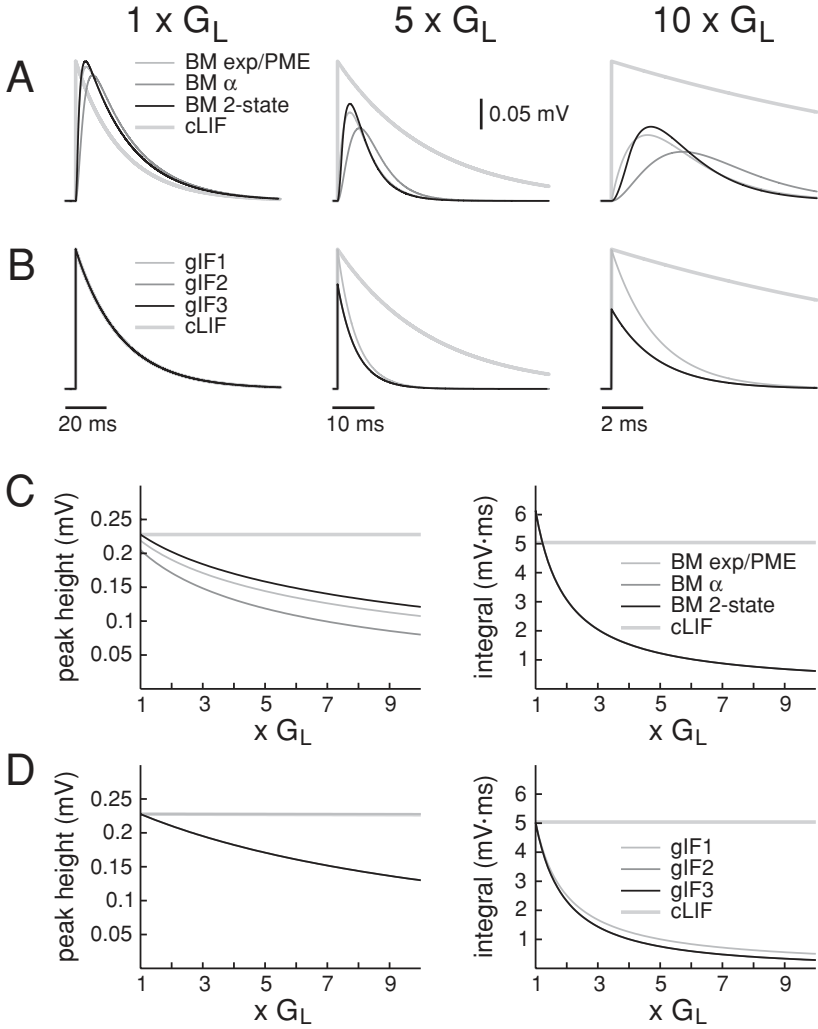$$G_m(t) = G_L + G_s(t) \qquad\qquad (2.3)$$

(see Figure 2A, top), which determines the amplitude and shape of postsynaptic potentials (PSPs) and, hence, the response of the cellular membrane to subsequent synaptic inputs.

We will restrict what follows to two direct consequences of changes in the membrane conductance caused by synaptic activity. First, a change in G_m results in a change of the membrane time constant τ_m of the form

$$\tau_m(t) = \frac{C}{G_m(t)}, \qquad\qquad (2.4)$$

where C denotes the membrane capacity (see Figure 2A, middle). This leads to an alteration in the membrane integration time and, therefore, the shape of the PSPs (see Figure 2A, bottom). For larger G_m, the PSP rising and decay times will be shorter, whereas a lower G_m results in a slower membrane. Second, a change in the membrane conductance will also result in a change of the PSP peak height and, thus, the amplitude of the subthreshold cellular response to synaptic stimulation.

Figure 1: Comparison of excitatory postsynaptic potentials (EPSPs) for different neuron models. (A) The EPSP time course in biophysical models described by a passive membrane equation with synaptic input following exponential time course (BM exp/PME), α-kinetics (BM α), and two-state kinetics (BM 2-state) are compared to that in a corresponding classic LIF neuron model (cLIF) for three different total membrane conductances ($1 \times G_L, 5 \times G_L, 10 \times G_L; G_L = 17.18$ nS corresponding to $\tau_m^L = 22.12$ ms). (B) Comparison of the EPSP time course for the gIF models for membrane conductances as in A. (C) EPSP peak height (left) and integral over the EPSP peak (right) for biophysical models as a function of the total membrane conductance, given in multiples of G_L. Whereas the EPSP shape in classical IF neuron models (cLIF) remains constant, both the EPSP peak height and integral decrease for increasing membrane conductance for the biophysical models. (D) EPSP peak height (left) and integral over EPSP peak (right) for the gIF models. Whereas the peak amplitude stays constant for the gIF1 model, the decrease in the EPSP integral for this model as well as the functional dependence of the peak height and integral for the gIF2 and gIF3 model compare well to the detailed models shown in C. Computational models are described in appendix A; time courses of synaptic conductances and used parameters are given in Tables 1 and 2.

A
- BM exp/PME
- BM α
- BM 2-state
- cLIF

B
- gIF1
- gIF2
- gIF3
- cLIF

C
- BM exp/PME
- BM α
- BM 2-state
- cLIF

D
- gIF1
- gIF2
- gIF3
- cLIF

Generalizations of the IF model incorporating a time-dependent, more precisely a spike-time-dependent (Wehmeier, Dong, Koch, & van Essen, 1989; LeMasson, Marder, & Abbott, 1993; Stevens & Zador, 1998a; Giugliano, Bove, & Grattarola, 1999; Jolivet, Lewis, & Gerstner, 2004), membrane time constant, have already been investigated in the context of the spike response model (e.g., Gerstner & van Hemmen, 1992, 1993; Gerstner, Ritz, & van Hemmen, 1993; Gerstner & Kistler, 2002). In this case, right after a postsynaptic spike, the membrane conductance is increased due to the contribution of ion channels linked to the spike generation. This leads to a reduction of the membrane time constant immediately after a spike, which shapes the amplitude and form of subsequent postsynaptic potentials (for experimental studies showing a dependence of the PSP shape on intrinsic membrane conductances, see, e.g., Nicoll, Larkman, & Blakemore, 1993; Stuart & Spruston, 1998). However, in contrast to the spike response model in which the membrane time constant is a function of the time since the last postsynaptic spike and, hence, the postsynaptic activity, in this article the time dependence results directly from synaptic inputs and, hence, is a consequence of the overall presynaptic activity.

To study in more detail the scaling properties of the PSPs as a function of the total membrane conductance, we investigated the peak amplitude and integral of excitatory postsynaptic potentials (EPSPs) as a function of a static membrane conductance G_L for different models of postsynaptic

---

Figure 2: Integrate-and-fire models with presynaptic-activity dependent state dynamics. (A) Synaptic inputs lead to transient changes in the total membrane conductance G_m that depend on the synaptic kinetics and release statistics. Exponential synapses, for instance, cause an instantaneous increase in the G_m, followed by an exponential decay back to its resting (leak) value (left, top). This change in G_m is paralleled by a transient change in the effective membrane time constant τ_m (left, middle), and change in the membrane state variable m (left, bottom). At high synaptic input rates (right), the membrane is set into a high-conductance state with rapidly fluctuating membrane conductance and, hence, membrane time constant. The resulting high-amplitude variations of the membrane state variable m resemble those found in vivo during active network states. (B) Comparison of high-conductance dynamics in the passive biophysical model with two-state synaptic kinetics (BM), the classical LIF neuron model (cLIF), and the gIF models (bottom). In each panel, the upper trace shows a 500 ms time course of the membrane time constant and the lower trace the corresponding membrane state time course. The gIF3 model comes closest to the dynamics seen in the detailed model. Computational models are described in appendix A; time courses of synaptic conductances and used parameters are given in Tables 1 and 2. Input rates were 10 Hz (A, left), 6 kHz (A, right), and 3 kHz (B).
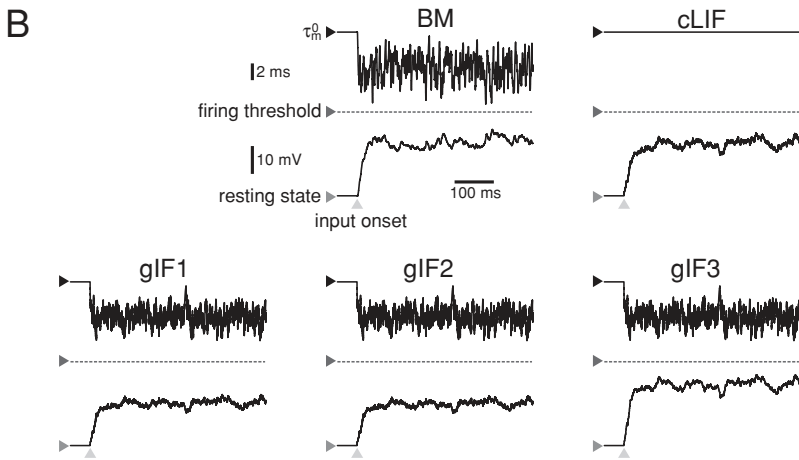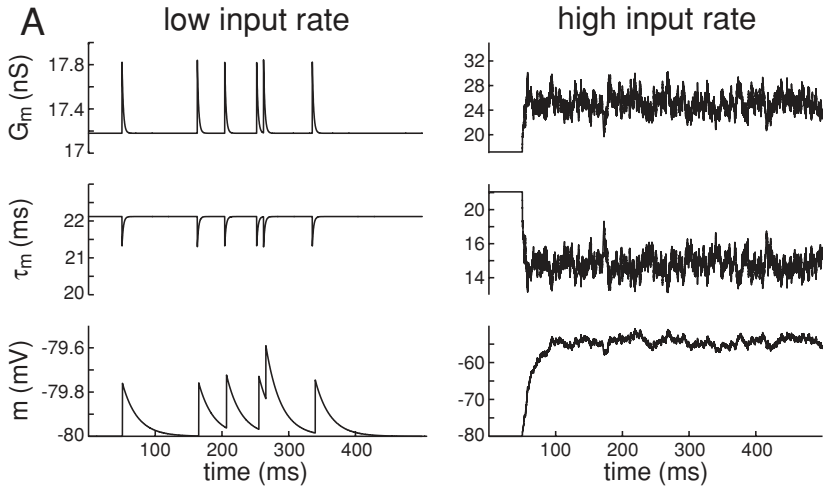
A

low input rate

high input rate

B

Table 1: Models and Parameters of Postsynaptic Membrane Conductances.

	Exponential Synapse	α-Synapse	Two-State Kinetics
Conductance time course	$G_s^{\mathrm{exp}}(t) = \overline{G}\,e^{-\frac{t}{\tau_s}}$	$G_s^{\alpha}(t) = \overline{G}\,\frac{t}{\tau_s}\,e^{-\frac{t}{\tau_s}}$	$G_s^{2s}(t) =$ $\begin{cases} \overline{G}r_\infty\left(1 - e^{-tA}\right) \\ \text{for } 0 \le t < t_{dur} \\ \overline{G}r(t_{dur})\,e^{-\beta(t-t_{dur})} \\ \text{for } t_{dur} \le t < \infty \end{cases}$
Total conductance per quantal event	$G_{total}^{\mathrm{exp}} = \overline{G}\,\tau_s$	$G_{total}^{\alpha} = \overline{G}\,\tau_s$	$G_{total}^{2s} =$ $\frac{\overline{G}T_{\max}\alpha}{A^2\beta} \times \{\beta t_{dur}\,A + \alpha T_{\max} - \alpha T_{\max}e^{-t_{dur}\,A}\}$
Excitatory conductance parameters	$\overline{G} = 0.66$ nS $\tau_s = 2$ ms	$\overline{G} = 0.66$ nS $\tau_s = 2$ ms	$\overline{G} = 1.2$ nS $\alpha = 1.1\ (\mathrm{ms\ mM})^{-1}$ $\beta = 0.67\ \mathrm{ms}^{-1}$ $T_{\max} = 1$ mM $t_{dur} = 1$ ms
Inhibitory conductance parameters	$\overline{G} = 0.632$ nS $\tau_s = 10$ ms	$\overline{G} = 0.632$ nS $\tau_s = 10$ ms	$\overline{G} = 0.6$ nS $\alpha = 5\ (\mathrm{ms\ mM})^{-1}$ $\beta = 0.1\ \mathrm{ms}^{-1}$ $T_{\max} = 1$ mM $t_{dur} = 1$ ms

Notes: The conductance time course, total quantal conductance, and conductance parameters used in this study are given for exponential synapses, α-synapses, and synapses described by (pulse-based) two-state kinetic models (Destexhe et al., 1994, 1998; see section A.1 for definitions). For simplicity, the time of the release t_0 was set to 0. $\overline{G}$ denotes the maximal conductance and τ_s the time constant describing the synaptic kinetics. In the two-state kinetic model, t_{dur} is the duration of transmitter release, and $r_\infty = \frac{\alpha T_{\max}}{A}$ with $A = \beta + \alpha T_{\max}$, where $T_{\max}$ denotes the transmitter concentration, α and β the forward and backward transmitter binding rates, respectively. Conductance parameters for the different models were chosen to yield the same total conductance: $G_{total}^{\mathrm{exp}} = G_{total}^{\alpha} = G_{total}^{2s}$.

conductance dynamics (exponential synapse; α-synapse, see Rall, 1967; synapse with two-state kinetics, see Destexhe, Mainen, & Sejnowski, 1994, 1998; computational models are described in appendix A). In all models, the parameters were adjusted to yield the same total conductance applied to the membrane for individual synaptic inputs (see Table 1). As expected, the EPSP peak height declines for increasing membrane conductance, with absolute amplitude and shape depending on the kinetic model used (see Figures 1A and 1C, left). The integral over the EPSP was much less dependent on the kinetic model, a consequence of the equalized total conductance for each synaptic event, but decreased markedly for increasing G_L (see Figure 1C, right).

In the LIF neuron model, neither of these effects seen in the biophysical model and experiments occurs. Both the EPSP peak height and the integral over the EPSP (determined by the membrane time constant) are constant (see Figures 1A and 1C). The question arising now is which modifications or extensions of the LIF neuron model can account for EPSP peak height and EPSP integral as functions of the membrane conductance. In what follows we will present such extensions. The constructed models will be called *conductance-based (g-based) integrate-and-fire neuron models*, which we refer to as *gIF neuron models*.

2.3 gIF1—The Basic gIF Model. We consider the simplest transient change in the total membrane conductance after a synaptic input, namely, the exponential synapse. At the arrival of a synaptic event at time t_0, the synaptic contribution to G_m (see equation 2.3) rises instantaneously by a constant value ΔG_s and decays afterward exponentially with time constant τ_s to zero until the arrival of a new synaptic event at time t_1:

$$G_s(t_0) \longrightarrow G_s(t_0) + \Delta G_s ,$$

$$G_s(t) = G_s(t_0)\, e^{-\frac{t-t_0}{\tau_s}} \qquad \text{for } t_0 \le t < t_1. \tag{2.5}$$

Due to the additivity of conductances for this model, equations 2.5 hold also for multiple synaptic inputs. This yields, in general, an average synaptic contribution to the membrane conductance whose statistical properties, such as mean, variance, or spectral properties, are determined by the statistics and functional properties of quantal synaptic release events (Rudolph & Destexhe, 2005).

Due to the correspondence between membrane conductance and membrane time constant (see equation 2.4), equations 2.5 can be translated into corresponding changes in τ_m. The state of the membrane at time t is characterized by a membrane time constant $\tau_m(t)$ obeying

$$\frac{1}{\tau_m(t)} = \frac{1}{\tau_m^L} + \frac{1}{\tau_m^s(t)}, \tag{2.6}$$

where $\tau_m^L = C/G_L$ denotes the membrane time constant at the resting state without synaptic activity and $\tau_m^s(t) = C/G_s(t)$ the time-varying time constant due to synaptic conductances. After the arrival of a synaptic input, τ_m^s rises instantaneously by $\Delta \tau_m^s = C/\Delta G_s$,

$$\frac{1}{\tau_m^s(t_0)} \longrightarrow \frac{1}{\tau_m^s(t_0)} + \frac{1}{\Delta \tau_m^s} . \tag{2.7}$$

Due to the decay of G_s given in equation 2.5, the membrane time constant τ_m increases ("decays") after this change back to its resting value τ_m^L

according to

$$\frac{1}{\tau_m(t)} = \frac{1}{\tau_m^L} + \frac{1}{\tau_m^s(t_0)} \, e^{-\frac{t-t_0}{\tau_s}} \qquad \text{for } t_0 \le t < t_1. \tag{2.8}$$

This well-known translation of membrane conductance changes due to synaptic activity into corresponding changes in the membrane time constant now provides a simple way to incorporate the effect of conductance-based synaptic activity into the IF neuron model framework. Replacing the membrane time constant τ_m in the LIF model, equation 2.1, by the time-dependent membrane time constant $\tau_m(t)$ given by equation 2.8, yields

$$\tau_m(t) \frac{dm(t)}{dt} + m(t) = 0, \tag{2.9}$$

which describes the evolution of the neuronal state variable between two synaptic arrivals. Equation 2.9 can be solved explicitly, leading to

$$m(t) = m(t_0) \exp\left[-\frac{t-t_0}{\tau_m^L} - \frac{\tau_s}{\tau_m^s(t_0)} \left(1 - e^{-\frac{t-t_0}{\tau_s}} \right) \right], \tag{2.10}$$

where $m(t_0)$ and $\tau_m^s(t_0)$ are the membrane state and the synaptic contribution to the membrane time constant after the last synaptic input at time t_0. This solution defines the core of the gIF models considered in this article. The apparent difference to the LIF neuron model is that now the state variable $m(t)$ decays with an effective time constant that is no longer constant but depends on the overall synaptic activity.

In contrast to the synaptic input modulated membrane dynamics in between synaptic events, the membrane state $m(t)$ is still updated by a constant value Δm upon arrival of a synaptic input, that is,

$$m(t_0) \longrightarrow m(t_0) + \Delta m. \tag{2.11}$$

This corresponds to a constant PSP peak amplitude, independent of the current membrane state (see Figure 1D, left). However, due to the state-dependent membrane time constant, the decay and, hence, shape of the PSP will depend on the level of synaptic activity (see Figure 1B). This dependence reflects in the change of the integral over the PSP, which decreases with decreasing average membrane time constant and matches closely the values observed in conductance-based models of synaptic kinetics (see Figure 1; compare Figures 1C and 1D, right). We note that in subsequent gIF models introduced in the following sections, the constant Δm in equation 2.11 will be replaced by expressions that capture the effect of a state-dependent scaling of the PSP peak amplitude.

So far, only one conductance component and its impact on the membrane time constant was considered (see equation 2.6). However, many studies in anesthetized animals (e.g., Borg-Graham, Monier, & Frégnac, 1998; Hirsch, Alonso, Reid, & Martinez, 1998; Paré, Shink, Gaudreau, Destexhe, & Lang, 1998; for a review, see Destexhe et al., 2003), as well as during wakefulness and natural sleep periods, have directly shown that both excitatory and inhibitory synaptic conductance contributions shape the state of the cellular membrane. Generalizing equations 2.5 to 2.10 to the situation of independent excitatory and inhibitory synaptic inputs, we finally obtain a set of state equations that define the dynamics of the gIF1 model. Specifically, the inverse membrane time constant is a sum of resting state as well as excitatory and inhibitory synaptic contributions:

$$\frac{1}{\tau_m(t)} = \frac{1}{\tau_m^L} + \frac{1}{\tau_m^e(t)} + \frac{1}{\tau_m^i(t)}. \tag{2.12}$$

It "decays" with two different time constants τ_e and τ_i for excitatory and inhibitory synaptic conductances, respectively, to its resting value τ_m^L,

$$\frac{1}{\tau_m(t)} = \frac{1}{\tau_m^L} + \frac{1}{\tau_m^e(t_0)} \, \mathrm{e}^{-\frac{t-t_0}{\tau_e}} + \frac{1}{\tau_m^i(t_0)} \, \mathrm{e}^{-\frac{t-t_0}{\tau_i}}. \tag{2.13}$$

With this, the solution of equation 2.9 is given by

$$m(t) = m(t_0) \exp\left[-\frac{t-t_0}{\tau_m^L} - \frac{\tau_e}{\tau_m^e(t_0)} \left(1 - \mathrm{e}^{-\frac{t-t_0}{\tau_e}}\right) - \frac{\tau_i}{\tau_m^i(t_0)} \left(1 - \mathrm{e}^{-\frac{t-t_0}{\tau_i}}\right) \right], \tag{2.14}$$

where $\tau_m^e(t_0)$ and $\tau_m^i(t_0)$ are the excitatory and inhibitory synaptic contributions to the membrane time constant at time t_0. Upon arrival of a synaptic event at time t_0, the state variable and synaptic contributions of the membrane time constant are updated according to

$$m(t_0) \longrightarrow m(t_0) + \Delta m_{\{e,i\}}, \tag{2.15}$$

$$\frac{1}{\tau_m^{\{e,i\}}(t_0)} \longrightarrow \frac{1}{\tau_m^{\{e,i\}}(t_0)} + \frac{1}{\Delta \tau_m^{\{e,i\}}}, \tag{2.16}$$

where the indices e and i denote excitatory and inhibitory synaptic inputs, respectively.

2.4 gIF2—An Extended gIF Model. So far we have considered the effect of synaptic activity only on the membrane time constant τ_m, whereas the amplitude of individual synaptic events was kept constant. In other words,

the update of the state variable $m(t)$ by Δm at the arrival of an synaptic event (equations 2.11 and 2.15) was independent of the presynaptic activity. However, for equal synaptic conductance time course and membrane state, a leakier and, hence, faster membrane will result in an effective reduction of the PSP amplitude (see Figures 1A and 1C, left). To extend the gIF1 model in this direction, we analytically solved the membrane equation for a single synaptic input event described by an exponential conductance time course (see section B.1) and approximated the obtained explicit expression for the PSP time course by an α-function (see section B.2). This yields for the update $\Delta m(\tau_m(t_0))$ of the membrane state variable $m(t)$ due to the arrival of a synaptic input at time t_0

$$m(t_0) \longrightarrow m(t_0) + \Delta m(\tau_m(t_0)), \tag{2.17}$$

with

$$\Delta m(\tau_m(t_0)) = \Delta \tilde{m}(\tilde{\tau}_m) \left(\frac{1}{\tilde{\tau}_m} + \frac{1}{\tau_s} + \frac{1}{\Delta \tau_m^s} \right) \left(\frac{1}{\tau_m(t_0)} + \frac{1}{\tau_s} + \frac{1}{\Delta \tau_m^s} \right)^{-1}. \tag{2.18}$$

Here, $\tau_m(t_0)$ denotes the actual membrane time constant at the time of the synaptic event, and $\Delta \tilde{m}(\tilde{\tau}_m)$ is the reference value for the PSP peak amplitude in a control state characterized by the membrane time constant $\tilde{\tau}_m$ (see section B.2). Throughout the text and in all numerical simulations, this state was taken to be the resting state at $m = m_L = 0$, that is, $\tilde{\tau}_m \equiv \tau_m^L$.

Equations 2.17 and 2.18 can be generalized to independent excitatory and inhibitory synaptic input channels. In this case, the membrane state variable $m(t)$ is subject to an update

$$m(t_0) \longrightarrow m(t_0) + \Delta m_{\{e,i\}}(\tau_m(t_0)), \tag{2.19}$$

with

$$\Delta m_{\{e,i\}}(\tau_m(t_0)) = \Delta \tilde{m}_{\{e,i\}}(\tilde{\tau}_m) \left(\frac{1}{\tilde{\tau}_m} + \frac{1}{\tau_{\{e,i\}}} + \frac{1}{\Delta \tau_m^{\{e,i\}}} \right)$$
$$\times \left(\frac{1}{\tau_m(t_0)} + \frac{1}{\tau_{\{e,i\}}} + \frac{1}{\Delta \tau_m^{\{e,i\}}} \right)^{-1}. \tag{2.20}$$

These equations describe the scaling of the PSP peak amplitude depending on the actual membrane conductance (see Figure 1) and define together with equations 2.12, 2.13, and 2.14 the dynamics of the gIF2 model.

2.5 gIF3—A gIF Model with Synaptic Reversal Potentials. Barrages of synaptic inputs not only modulate the membrane time constant, but also

result in a change of the actual membrane state variable due to the presence of reversal potentials for synaptic conductances. In this case, excitatory synaptic inputs push the membrane closer to firing threshold, whereas inhibitory inputs in general will have the opposite effect. The average membrane potential is determined by the actual values of inhibitory and excitatory conductances, as well as the leak conductance, and their respective reversal potentials. To account for this effect, we extend the defining equation for the LIF model, equation 2.9, by an actual "effective reversal state" m_{rest} (e.g., see Borg-Graham et al., 1998; Shelley et al., 2002) to which the state variable $m(t)$ decays with the membrane time constant $\tau_m(t)$ (see section B.3):

$$\tau_m(t) \frac{dm(t)}{dt} + \left(m(t) - m_{rest}\right) = 0. \tag{2.21}$$

Here, $\tau_m(t)$ is given by equation 2.8 and

$$m_{rest} = \left(\frac{m_L}{\tau_m^L} + \frac{m_s}{\tau_m^s(t_0)}\right)\left(\frac{1}{\tau_m^L} + \frac{1}{\tau_m^s(t_0)}\right)^{-1}, \tag{2.22}$$

where m_L denotes the true resting (leak reversal) state in the absence of synaptic activity (usually assumed to be $m_L = 0$), and m_s is the value of the state variable corresponding to the synaptic reversal. Note that in order to allow a solution of equation B.3, m_{rest} is assumed to stay constant between two synaptic inputs. When a new synaptic event arrives, m_{rest} is updated according to equation 2.22 with a new value for τ_m^s, thus endowing m_{rest} with an indirect time dependence.

Equation 2.21, which describes the evolution of the neuronal state variable between two synaptic inputs in the presence of a synaptic reversal potential, can be explicitly solved, yielding

$$m(t) = m_{rest} + \left(m(t_0) - m_{rest}\right) \exp\left[-\frac{t - t_0}{\tau_m^L} - \frac{\tau_s}{\tau_m^s(t_0)}\left(1 - e^{-\frac{t-t_0}{\tau_s}}\right)\right]. \tag{2.23}$$

In the case of excitatory and inhibitory synaptic inputs, this solution generalizes to

$$m(t) = m_{rest} + \left(m(t_0) - m_{rest}\right) \exp\left[-\frac{t - t_0}{\tau_m^L} - \frac{\tau_e}{\tau_m^e(t_0)}\left(1 - e^{-\frac{t-t_0}{\tau_e}}\right) \right.$$
$$\left. - \frac{\tau_i}{\tau_m^i(t_0)}\left(1 - e^{-\frac{t-t_0}{\tau_i}}\right)\right], \quad (2.24)$$

with the generalized effective reversal state variable

$$m_{rest} = \left(\frac{m_L}{\tau_m^L} + \frac{m_e}{\tau_m^e(t_0)} + \frac{m_i}{\tau_m^i(t_0)}\right)\left(\frac{1}{\tau_m^L} + \frac{1}{\tau_m^e(t_0)} + \frac{1}{\tau_m^i(t_0)}\right)^{-1}. \qquad (2.25)$$

Finally, the change in the membrane state variable due to synaptic inputs will bring the membrane closer to or farther away from the corresponding synaptic reversal potential, thus yielding a change of the synaptic current linked to the synaptic events. The latter results in an additional modulation of the PSP peak amplitude (see Figure 3A), which appears to be particularly important for inhibitory synaptic inputs. Because the synaptic reversal potential lies in general between the resting state and the firing threshold, inhibitory inputs can have both a depolarizing and hyperpolarizing effect as the membrane state increases from its resting value to firing threshold (see Figures 3A right and 3C left).

To incorporate this effect in the gIF3 model, we extended the solution of the full membrane equation for a single exponential synaptic input (see section B.3). From this we obtain a simple explicit expression for the PSP peak amplitude, hence the update $\Delta m(\tau_m(t_0), m(t_0))$ of $m(t)$ at arrival of a synaptic input at time t_0, as a function of both the actual total membrane conductance and the actual membrane state (hence, the actual distance to the reversal state):

$$m(t_0) \longrightarrow m(t_0) + \Delta m(\tau_m(t_0), m(t_0)), \qquad (2.26)$$

with

$$\Delta m(\tau_m(t_0), m(t_0)) = \Delta \tilde{m}(\tilde{\tau}_m, \tilde{m}) \frac{m(t_0) - m_s}{\tilde{m} - m_s}\left(\frac{1}{\tilde{\tau}_m} + \frac{1}{\tau_s} + \frac{1}{\Delta\tau_m^s}\right)$$

$$\times \left(\frac{1}{\tau_m(t_0)} + \frac{1}{\tau_s} + \frac{1}{\Delta\tau_m^s}\right)^{-1}, \qquad (2.27)$$

where $\Delta\tilde{m}(\tilde{\tau}_m, \tilde{m})$ denotes the reference value for the PSP peak amplitude in a control state characterized by the membrane time constant $\tilde{\tau}_m$ and membrane state $\tilde{m}$ (taken to be the resting state at $m = m_L = 0$), and m_s is the value of the state variable corresponding to the synaptic reversal.

Generalizing the model to scope with both excitatory and inhibitory synaptic inputs, equations 2.26 and 2.27 take the form

$$m(t_0) \longrightarrow m(t_0) + \Delta m_{\{e,i\}}(\tau_m(t_0), m(t_0)), \qquad (2.28)$$
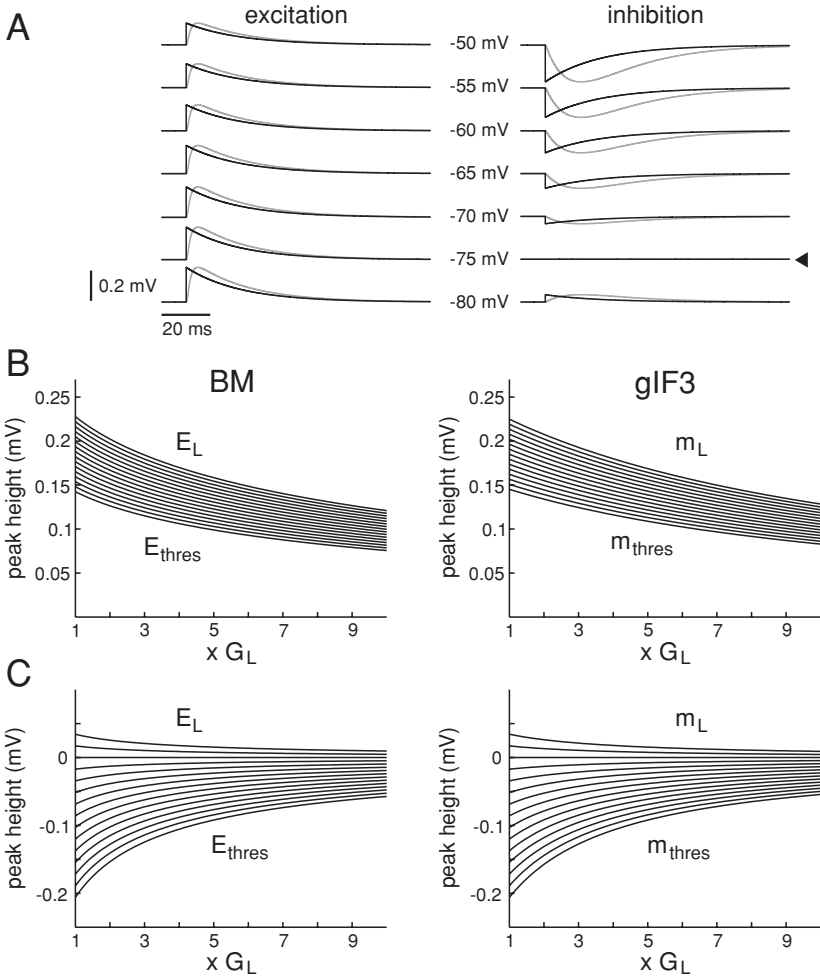
with

Figure 3: Excitatory and inhibitory postsynaptic potentials. (A) Comparison of EPSPs (left) and IPSPs (right) in the two-state kinetic model (gray) and gIF3 model (black) for different membrane potentials. The arrow marks the reversal potential for inhibition. (B) EPSP peak height for the two-state kinetic model (left) and gIF3 model (right) as a function of the total membrane conductance, given in multiples of the leak conductance $G_L = 17.18$ nS, for different membrane potentials ranging from the leak reversal (E_L and m_L, respectively) to the firing threshold E_{thres} and m_{thres}, respectively. (C) Comparison of IPSP peak heights for the two-state kinetic model (left) and gIF3 model (right) as a function of the total membrane conductance and different membrane potentials as in B. Used parameters of synaptic kinetics and the time course of synaptic conductances are given in Tables 1 and 2. The membrane state values in the gIF3 model were normalized as described in section A.3.

$$\Delta m_{\{e,i\}}(\tau_m(t_0), m(t_0)) = \Delta \tilde{m}_{\{e,i\}}(\tilde{\tau}_m, \tilde{m}) \, \frac{m(t_0) - m_{\{e,i\}}}{\tilde{m} - m_{\{e,i\}}}$$

$$\times \left(\frac{1}{\tilde{\tau}_m} + \frac{1}{\tau_{\{e,i\}}} + \frac{1}{\Delta \tau_m^{\{e,i\}}} \right)$$

$$\times \left(\frac{1}{\tau_m(t_0)} + \frac{1}{\tau_{\{e,i\}}} + \frac{1}{\Delta \tau_m^{\{e,i\}}} \right)^{-1}, \qquad (2.29)$$

where $m_{\{e,i\}}$ denotes the synaptic reversal state variable for excitation (index e) and inhibition (index i), respectively. The two last equations, together with equations 2.12, 2.13, 2.24, and 2.25, define the dynamics of the gIF3 model. Due to the incorporation of the effect of the synaptic reversal states, the gIF3 model is the most realistic of the introduced gIF models with presynaptic-activity dependent state dynamics and state-dependent synaptic input amplitude, and describes best the behavior seen in the biophysical model (see Figures 1 and 3).

3 Response Dynamics of gIF models

In this section, we compare the spiking response dynamics of the introduced gIF models with presynaptic-activity dependent state dynamics to that of biophysical models with multiple synaptic inputs described by two-state kinetics, to the passive membrane equation with exponential conductance-based synapses and fixed spike threshold, as well as with the behavior seen in leaky IF neuron models. In the following section, we first characterize the statistics of spontaneous discharge activity. In section 3.2, we study the temporal resolution of synaptic inputs in the different models. Finally, in section 3.3, we investigate the modulatory effect of synaptic inputs on the cellular gain. Computational models are described in appendix A, with parameters provided in Tables 1 and 2.

3.1 Spontaneous Discharge Statistics. Spontaneous discharge activity in the investigated models was evoked by Poisson-distributed random release at excitatory and inhibitory synaptic terminals with stationary rates that were selected independently in a physiologically relevant parameter regime (see appendix A). In the biophysical model, 10,000 input channels for excitatory and 3000 for inhibitory synapses releasing in a range from 0 to 10 Hz each were used, thus yielding total input rates from $\nu_e = 0$ to 100 kHz for excitation and from $\nu_i = 0$ to 30 kHz for inhibition (see section A.1). The cell's output rate (ν_{out}) increased gradually for increasing ν_e up to 300 Hz for extreme excitatory drive (see Figure 4, BM). Moreover, in the investigated input parameter regime, a nearly linear relationship between excitatory and inhibitory synaptic release rates yielding comparable output rates, indicated by a linear behavior of the equi-ν_{out} lines, was observed.

Table 2: Parameter Values for Integrate-and-Fire Neuron Models.

	cLIF/vLIF	gIF1	gIF2	gIF3
Membrane properties	$\tau_m^L = 22.12$ ms ($\tau_m^L = 4.42$ ms)	$\tau_m^L = 22.12$ ms	$\tau_m^L = 22.12$ ms	$\tau_m^L = 22.12$ ms $m_L = 0$
Excitatory inputs	$\Delta m_e = 0.0095$	$\Delta m_e = 0.0095$ $\tau_e = 2$ ms $\Delta\tau_m^e = 575.96$ ms	$\Delta m_e = 0.0095$ $\tau_e = 2$ ms $\Delta\tau_m^e = 575.96$ ms	$\Delta m_e = 0.0076$ $\tau_e = 2$ ms $\Delta\tau_m^e = 575.96$ ms $m_e = 2.667$
Inhibitory inputs	$\Delta m_i = -0.0072$	$\Delta m_i = -0.0072$ $\tau_i = 10$ ms $\Delta\tau_m^i = 601.3$ ms	$\Delta m_i = -0.0072$ $\tau_i = 10$ ms $\Delta\tau_m^i = 601.3$ ms	$\Delta m_i = 0.0014$ $\tau_i = 10$ ms $\Delta\tau_m^i = 601.3$ ms $m_i = 0.167$

Notes: Values for the passive (leak) membrane time constant τ_m^L, excitatory and inhibitory synaptic time constants (τ_e and τ_i, respectively), synaptic reversal states (m_e and m_i), as well as changes in the membrane state variables (Δm_e and Δm_i) and synaptic contributions to the membrane time constant ($\Delta\tau_m^e$ and $\Delta\tau_m^i$) for excitatory and inhibitory synaptic inputs, respectively, are given. For definitions, see section 2 and appendix A.

In the classic LIF (cLIF) neuron model, single independent input channels for excitatory and inhibitory synapses were used with rates that were downscaled by a factor of 5 compared to the total input rates in the biophysical model ($0 \leq \nu_e \leq 20$ kHz and $0 \leq \nu_i \leq 5$ kHz for excitatory and inhibitory inputs, respectively) to account for the larger membrane time constant (see section A.3). Although the firing rates were, in general, larger than for corresponding input values in the biophysical model, also here a linear dependence of the equi-ν_{out} lines was found (see Figure 4, cLIF). The latter suggests that inhibitory inputs play a less crucial role in determining the output rate.

A qualitatively similar behavior was also observed in the very leaky IF (vLIF) neuron model, which mimics a (static) high-conductance state by a small membrane time constant (see section A.3). In this case, two single independent input channels for excitatory and inhibitory inputs with rates equivalent to the total input rates in the biophysical model were used. Although the firing rates were, in general, larger than for corresponding input values in the cLIF as well as biophysical model (see Figure 4, vLIF), the linear dependence of ν_{out} on ν_e and ν_i corresponded qualitatively to that seen in both of these models, with a large slope as in the cLIF model. Both the overall higher output rates and the diminished modulatory effect of inhibitory inputs can be viewed as a direct consequence of a static membrane time constant or, equivalently, membrane conductance. This contrasts the situation seen in models driven with synaptic conductances, where the intensity of synaptic inputs determines the conductance state of the membrane. Here, at high input rates, the high membrane conductance will shunt
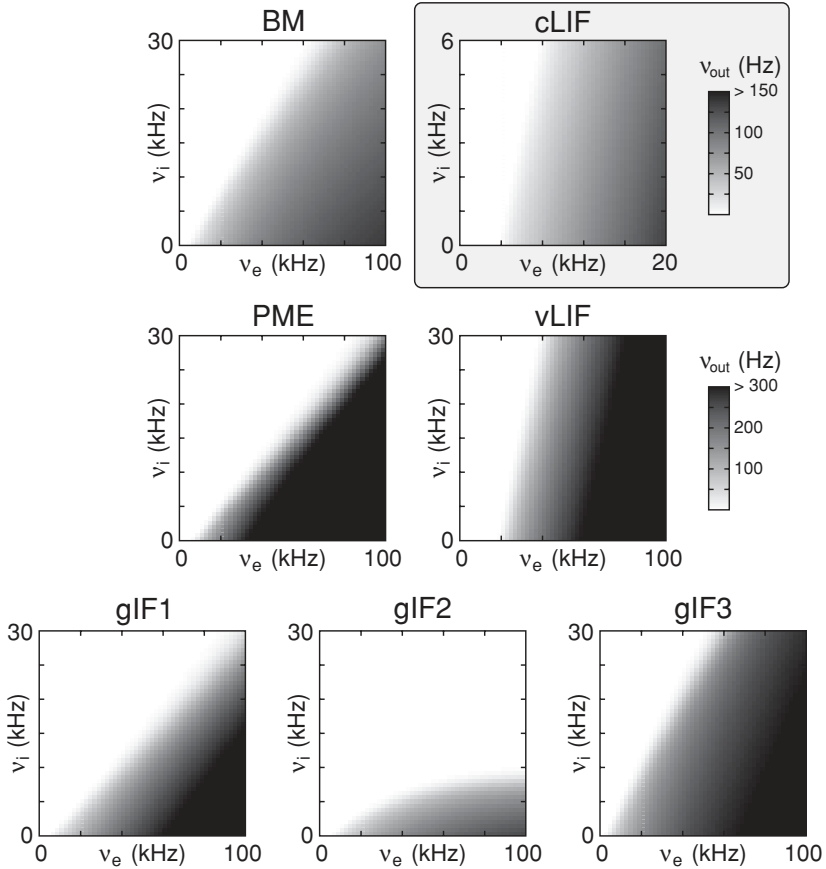
Figure 4: Spontaneous discharge rate as function of the total frequency of inhibitory and excitatory synaptic inputs. The biophysical model with two-state kinetic synapses (BM) is compared with the passive membrane equation (PME), the classical leaky and very leaky IF (with five times reduced membrane time constant) neuron models (cLIF and vLIF, respectively), as well as the gIF neuronal models with presynaptic-activity dependent state dynamics (gIF1, gIF2, gIF3). The synaptic input in the biophysical model consisted of 10,000 independent excitatory and 3000 independent inhibitory channels, releasing with individual rates between 0 and 10 Hz each. For all other models, two independent input channels for excitation and inhibition releasing at rates between 0 and 100 kHz (for excitation) and 0 and 30 kHz (for inhibition) were used (except for the leaky IF, in which case the rates varied between 0 and 20 kHz for excitation and 0 and 6 kHz for inhibition). Used parameters of synaptic kinetics and the time course of synaptic conductances are given in Tables 1 and 2 as well as appendix A.

the membrane and in this way effectively lower the impact of individual synaptic inputs. The latter results in lower average firing rates compared to models with smaller and fixed membrane conductance but comparable synaptic input drive.

The modulatory effect of inhibitory inputs for an equivalent synaptic input regime was larger in all gIF models (see Figure 4, gIF1 to gIF3). Specifically, in the gIF1 and gIF3 models, the slope of the equi-ν_{out} lines was smaller than in the LIF models. Indeed, the gIF3 model reproduced best the qualitative behavior seen in the biophysical model, with only the output rate being larger for comparable input settings. Major deviations from the behavior seen in the biophysical model were observed only for the gIF2 model. In this case, the equi-ν_{out} lines showed a nonlinear dependence on ν_e and ν_i, with firing rates that were markedly lower in most of the investigated parameter regime.

To explain this finding, we note that in the gIF2 model, only the impact of the total conductance state on the PSP peak amplitudes is incorporated, while the current value of the membrane state variable and, hence, the distance to synaptic reversal potentials is not considered (see section 2.4). In general, a higher membrane conductance, as seen for higher input rates of both excitation and inhibition, will yield smaller PSP amplitudes. On the other hand, as described in section A.3, the amplitude of the PSPs was adjusted to those seen in the biophysical model close to firing threshold. Here, EPSPs have a smaller amplitude due to the smaller distance to the excitatory reversal potential, whereas for IPSPs, the opposite holds. As observed in the gIF2 model, this will lead to an effective decrease, or asymptotic "saturation," of the firing rate, in particular for high input rates where the PSP peak amplitudes are rescaled to smaller values due to the shunting effect of the membrane. The output rate can be modulated by tuning the amplitude values for PSPs (not shown), but without qualitative change in the nonlinear behavior seen in Figure 4 (gIF2).

In order to decompose the effect of active and synaptic conductances on the discharge activity, simulations of the passive membrane equation with fixed spike threshold were performed (see section A.2). Interestingly, the slope of the equi-ν_{out} lines was much smaller than in the biophysical as well as gIF3 model, and the firing rate increased much faster beyond 300 Hz for increasing ν_e than in all other investigated models (see Figure 4, PME). This indicates that incorporating a realistic PSP shape alone without the transient effects of spike-generating conductances on the membrane time constant and spike threshold does not suffice to reproduce a realistic spontaneous discharge behavior. Surprisingly, the gIF3 model, although being dynamically simpler, reproduced the spiking behavior seen in the biophysical model much better (see Figure 4). A possible explanation for this observation might be that the instantaneous rise of the membrane state variable on arrival of a synaptic inputs mimics a marked transient increase in the total membrane conductance and, hence, a faster membrane due to spike generation. This instantaneous update could effectively relax

the lack of the temporal effect of active membrane conductances and thus lead to a behavior closer to that seen in the biophysical model.

To further characterize the statistics of the discharge activity in the different models, we calculated the coefficient of variation C_V, defined by

$$C_V = \frac{\sigma_{ISI}}{\overline{ISI}}, \tag{3.1}$$

where σ_{ISI} denotes the standard deviation of the interspike intervals (ISIs) and $\overline{ISI}$ the mean ISI. In all investigated models, higher firing rates led to a more regular discharge, that is, smaller C_V values (see Figure 5). However, whereas in the biophysical model and for the passive membrane equation the regime with high discharge variability was broad and increased for higher input rates (see Figure 5, BM and PME), C_V values around unity were obtained in the LIF models only for a very tight balance between inhibitory and excitatory drive. The latter depended in the investigated parameter regime only minimally on the input rates (see Figure 5, cLIF and vLIF). This finding of a tight balance is in agreement with previously reported results (e.g., Softky & Koch, 1993; Rudolph & Destexhe, 2003). Interestingly, no differences were observed between the cLIF and vLIF models, although the membrane time constant in the vLIF model was five times smaller than in the cLIF model, thus yielding a much faster decay of individual PSPs. This indicates that the required higher input rates for excitation and inhibition and the resulting quantitatively different random-walk process close to threshold in the vLIF model did not relax the requirement of a narrow tuning of the synaptic input rates.

Although qualitative differences were found among the gIF models, high C_V values were observed in a generally broader regime of input frequencies (see Figure 5, gIF1 to gIF3) when compared with the LIF models. The gIF3 model came closest to discharge behavior observed in the biophysical model. This is interesting, as it suggests that a biologically more realistic discharge statistics can indeed be obtained with a simple threshold model without involvement of complex conductance-based spike-generating mechanisms (Rudolph & Destexhe, 2003). Support of this was also found in simulations with the passive membrane equation, although here a generally broader input regime resulting in high C_V values as well as smaller slope of equi-C_V lines compared to the biophysical and gIF3 models were observed (see Figure 5, PME). The smaller slope of the equi-C_V lines in the gIF models compared to the LIF models further suggests that here inhibitory inputs can tune the neural discharge activity in a much broader range of driving excitatory inputs. However, comparing the results obtained for the gIF3 model with the behavior observed for the gIF1 and gIF2 model (see Figure 5, gIF1 and gIF2), both the incorporation of the state-dependent PSP amplitude and the effect of the reversal potential on the PSP amplitude are necessary conditions to reproduce the discharge statistics of the biophysical model.
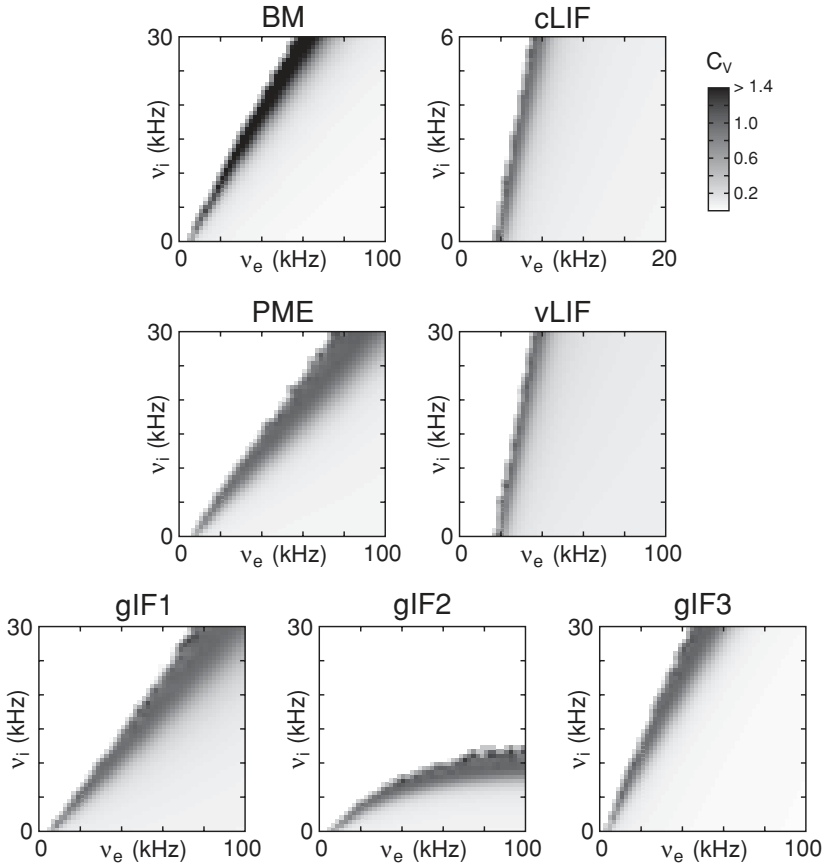
Figure 5: Coefficient of variation C_V as function of the total frequency of inhibitory and excitatory synaptic inputs. The C_V is defined as $C_V = \sigma_{ISI}/\overline{ISI}$, where σ_{ISI} denotes the standard deviation of the interspike intervals and $\overline{ISI}$ the mean interspike interval. The biophysical model with two-state kinetic synapses (BM) is compared with the passive membrane equation (PME), the classical leaky and very leaky IF (cLIF and vLIF, respectively), as well as the gIF models. Used parameters of synaptic kinetics, the time course of synaptic conductances, and synaptic release activity are the same as for Figure 4.

In order to fully reproduce the spontaneous discharge statistics seen in experiments (e.g., Smith & Smith, 1965; Noda & Adey, 1970; Burns & Webb, 1976; Softky & Koch, 1993; Stevens & Zador, 1998b), the high irregularity should also stem from a Poisson process; that is, the spike trains must be both exponentially distributed according to a gamma distribution and independent (Christodoulou & Bugmann, 2001; Rudolph & Destexhe, 2003).

Table 3: Specific Parameter Setup Used in Some of the Simulations.

	ν_e	ν_i	ν_{out}	C_V
BM	24 kHz	9.3 kHz	13.5 Hz	1.09
PME	30 kHz	8.2 kHz	12.8 Hz	0.96
cLIF	6 kHz	1.68 kHz	13.7 Hz	0.36
vLIF	26 kHz	8.4 kHz	12.5 Hz	0.80
gIF1	32 kHz	8.4 kHz	12.2 Hz	0.92
gIF2	40 kHz	6.0 kHz	11.9 Hz	0.95
gIF3	20 kHz	10.2 kHz	13.9 Hz	0.91

Notes: For all models, the synaptic input rates for excitation and inhibition (ν_e and ν_i, respectively) were chosen to yield an output rate ν_{out} of about 13 Hz, a high discharge variability C_V around 1 (except for cLIF and vLIF), and in the conductance-based models (BM, PME, gIF1, gIF2, gIF3) a total input conductance about five times larger than the leak conductance and comparable to the leak conductance of the vLIF model. For both the cLIF and vLIF models no combination of driving frequencies yields C_V values around 1 at an output rate of 13 Hz. Therefore, in the vLIF model, the input rates were chosen by taking the inhibitory rate of the gIF1 model and adjusting the excitatory rate to yield the desired output rate of about 13 Hz. For the cLIF model, the inhibitory input rate was then five times reduced and the excitatory rate adjusted to yield the same ν_{out}. Model descriptions are given in appendix A.

To test this, we chose for each model a synaptic activity that resulted in an average output rate around 13 Hz, a value consistent with the spontaneous discharge rate observed in cortical neurons in vivo (e.g., Evarts, 1964; Steriade & McCarley, 1990). Moreover, in order to account for experimental observations in the cortex in vivo (Borg-Graham et al., 1998; Paré et al., 1998), in all models except the cLIF model, synaptic activity was chosen to yield an about fivefold reduced membrane time constant compared to the leak time constant (see appendix A and Table 3).

In all cases, the ISI histograms (ISIHs) could be well fit with gamma distributions (see Figure 6). However, only in the biophysical and the gIF models, the behavior expected from a Poisson process, namely, gamma-distributed ISIs and a flat autocorrelogram (Figure 6, BM and gIF1 to gIF3), was accompanied by a high C_V value around unity (see Table 3). Indeed, the discharge in both the cLIF and vLIF models was much more regular, although the ISIHs resembled gamma distributions for the examples studied (Figure 6, cLIF and vLIF). Surprisingly, for both LIF models, no parameter setup in the investigated parameter space yielded both a high C_V and a desired output rate around 13 Hz at the same time. Moreover, the autocorrelogram in the LIF model showed a peak at small lag times (Figure 6, cLIF, star), indicating that subsequent output spikes were not independent. This behavior was mirrored in simulations of the PME model (Figure 6, PME). Here, despite the highly irregular discharge, a pronounced peak in the ISIH at small interspike intervals also suggests deviations from a spontaneous
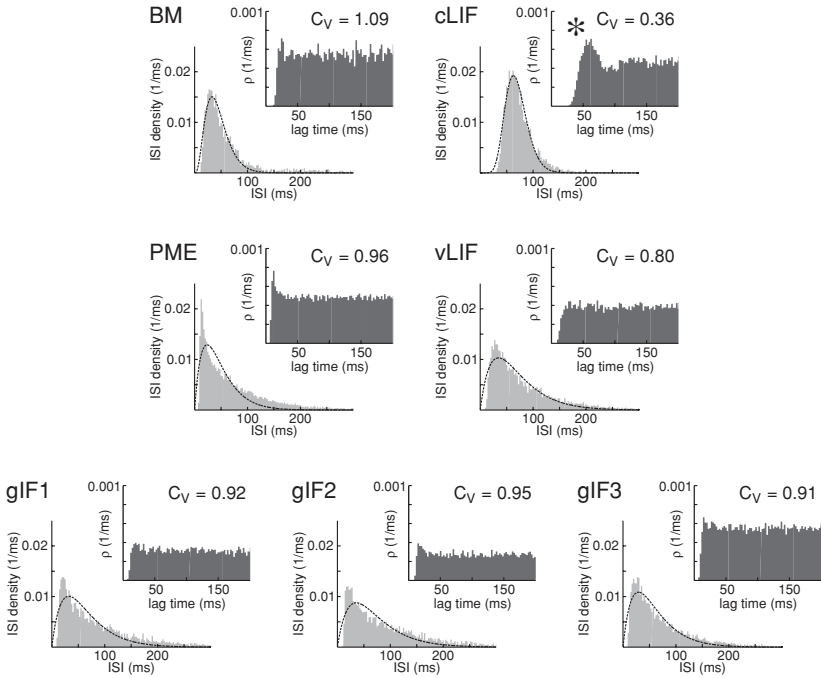
Figure 6: Typical interspike-interval histograms (ISIH) and autocorrelograms (insets) for the biophysical model (BM), the passive membrane equation (PME), the classical and very leaky IF (cLIF and vLIF, respectively) as well as the three gIF models. Synaptic input rates were chosen to yield comparable output rates and, except for the cLIF model, a five-fold decrease in input resistance compared to the quiescent case (see Table 3). ISIHs were fitted with gamma distributions $\rho_{ISI}(T) = \frac{1}{q!} a r (r T)^q e^{-rT}$, where $\rho_{ISI}(T)$ denotes the probability for occurrence of ISIs of length T and r, a, and q are parameters. Fitted parameters are: $q = 3$, $r = 0.091 \text{ ms}^{-1}, a = 0.737$ (BM); $q = 1, r = 0.042 \text{ ms}^{-1}, a = 0.824$ (PME); $q = 10$, $r = 0.159 \text{ ms}^{-1}, a = 0.965$ (cLIF); $q = 1, r = 0.029 \text{ ms}^{-1}, a = 0.970$ (vLIF); $q = 1, r = 0.031 \text{ ms}^{-1}, a = 0.873$ (gIF1); $q = 1, r = 0.028 \text{ ms}^{-1}, a = 0.845$ (gIF2); $q = 1, r = 0.034 \text{ ms}^{-1}, a = 0.868$ (gIF3).

discharge that is both independent and Poisson distributed, thus indicating limitations of a fixed threshold spike-generating mechanism to reproduce realistic discharge statistics.

Finally, it is interesting to note that in the ISIH of all models, a small peak for small ISIs was observed (see Figure 6). A possible explanation is that the models here are driven by uncorrelated synaptic inputs. In general, correlated input leads to an increase in the variability of the membrane state (Rudolph & Destexhe, 2005), which translates into a higher firing

rate. In order to obtain a desired output rate, the lack of correlation in the synaptic input has to be "compensated" for by an increase in the ratio between excitatory and inhibitory synaptic rates. The resulting pronounced excitatory drive causes volleys of "preferential" firing, which show up as peaks in the ISIH.

3.2 Temporal Resolution of Synaptic Inputs. As a second comparative test of the considered models, we investigated to what extent synaptic inputs could be temporally resolved. Due to a smaller membrane time constant and, hence, faster membrane in high-conductance states, a better temporal resolution of synaptic inputs is expected. To test this, we complemented a fixed background activity (see Table 3) with a suprathreshold periodic stimulus corresponding to a simultaneous activation of 30 synapses (6 synapses in the cLIF model). The frequency of the stimulus ν_{stim} was changed in successive trials between 1 and 200 Hz, corresponding to interstimulus intervals T_{stim} ranging from 1000 to 5 ms, respectively. The response of the cell to the periodic stimulus results in peaks at corresponding interspike intervals T_{ISI} in the ISIH (see Figure 7A). Due to limitations in the temporal resolution capability of the membrane and the related low-pass filtering of synaptic inputs, T_{ISI} will in general be larger than T_{stim}, especially for high-frequency stimuli. We used this "deviation" from the ideal situation, for which the stimulus would lead to a sharp peak in the ISIH at $T_{ISI} = T_{stim}$, as

Figure 7: Temporal resolution of periodic synaptic inputs. (A) In addition to Poisson synaptic inputs (see Table 3), a periodic stimulus of frequency ν_{stim} between 1 Hz and 200 Hz as well as an amplitude corresponding to the simultaneous activation of 30 synapses (6 synapse in the cLIF model) was used. The temporal resolution was quantified by computing the ratio between the stimulus interval T_{stim} and the mode of the corresponding ISIH at T_{ISI} (see equation 3.2). If multiple peaks were present in the ISIH (see Figure 8), the interspike interval T_{ISI} of the leading peak was used. (B) Output frequency ν_{out} as a function of ν_{stim} for the biophysical model (BM), the passive membrane equation (PME), the classical and very leaky IF (cLIF and vLIF, respectively), as well as the three gIF models. Compared to the biophysical model, the LIF neuron models yield much lower firing rates for all stimuli (left). Only in the gIF models were the output rates comparable to those observed in the biophysical model (right). (C) Temporal resolution as a function of stimulus frequency. For the chosen parameter setup, the LIF models were not able to resolve higher frequencies beyond 30 Hz (cLIF) and 80 Hz (vLIF; see left panel). Moreover, the temporal resolution changed in this model abruptly due to mode locking (see text). This behavior was not seen in the biophysical model and occurred in the gIF1 and gIF2 model (right) in a reduced fashion for high ν_{stim}. In contrast, the gIF3 model temporally resolved inputs above 120 Hz in a reliable fashion.

A

$$\text{temporal resolution} = \frac{T_{stim}}{T_{ISI}}$$

B

C
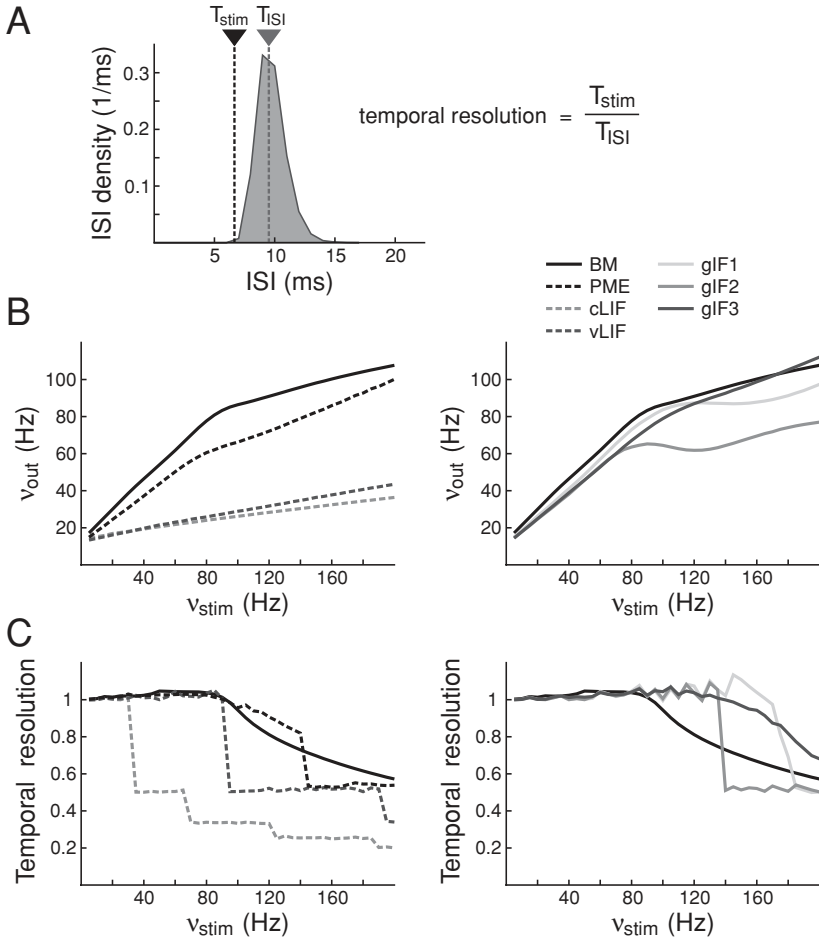
a measure of temporal resolution (Destexhe et al., 2003), namely,

$$\text{Temporal resolution} = \frac{T_{stim}}{T_{ISI}}. \qquad (3.2)$$

Already for the output rates ν_{out} as a function of the stimulus frequency, marked differences between the biophysical, PME and gIF models, on one hand, and the leaky IF neuron models, on the other hand, were found (see Figure 7B). In the conductance-based models, ν_{out} increased in coherence with the input frequency, $\nu_{out} \sim \nu_{stim}$, until an input frequency of about 80 Hz (see Figure 7B, solid lines). For the given parameter setup, this frequency marks the stimuli for which temporal resolution started to decrease (see below). In contrast, in the LIF models, the rise of the output rate as a function of ν_{stim} was much smaller and, surprisingly, nearly independent of the membrane time constant (see Figure 7B, dashed lines).

Larger membrane time constants impair the ability of the neuronal membrane to temporally resolve fast synaptic inputs. Theoretically, no inputs faster than the total membrane time constant can be reliably resolved, thus making the neuronal membrane a low-pass filter. In agreement with this, in the cLIF model, the temporal resolution dropped markedly at around 30 Hz (see Figure 7C, light gray dashed line), whereas the smaller membrane time constant in the vLIF model allowed resolving inputs up to 80 Hz (see Figure 7C, dark gray dashed line). Although the membrane time constant in the vLIF model corresponded to that in the biophysical model, in the latter case no sharp drop but a smooth decrease in the temporal resolution measure for increasing ν_{stim} was observed (compare the dark gray dashed and black solid lines in Figure 7C).

This abrupt change in the response behavior is typical for IF neurons and at least partially linked to the fixed firing threshold and current-based (i.e., not state-dependent) update of the membrane state upon arrival of a synaptic input or stimulus (for experimental and theoretical investigations, see, e.g., Brumberg, 2002; Fourcaud-Trocmé, Hansel, van Vreeswijk, & Brunel, 2003; Gutkin, Ermentrout, & Rudolph, 2003). The ISIH in the biophysical model showed up to 200 Hz only one wide peak (see Figure 8, BM, stars), indicating a reliable cellular response to the suprathreshold input, which is jittered around the stimuli due to the presence of random synaptic activity. This peak shifted toward smaller ISIs for increasing ν_{stim}. However, the higher the stimulating frequency, the more the low-pass property of the membrane determined the response, leading to a limit in the temporal resolution. Although at high ν_{stim} there was still a clear response of the cell (see Figure 8, BM, right), this response became increasingly decoupled from the stimulus in the sense that the cell spikes at a designated rate driven by the suprathreshold input, but independent of its temporal characteristics.
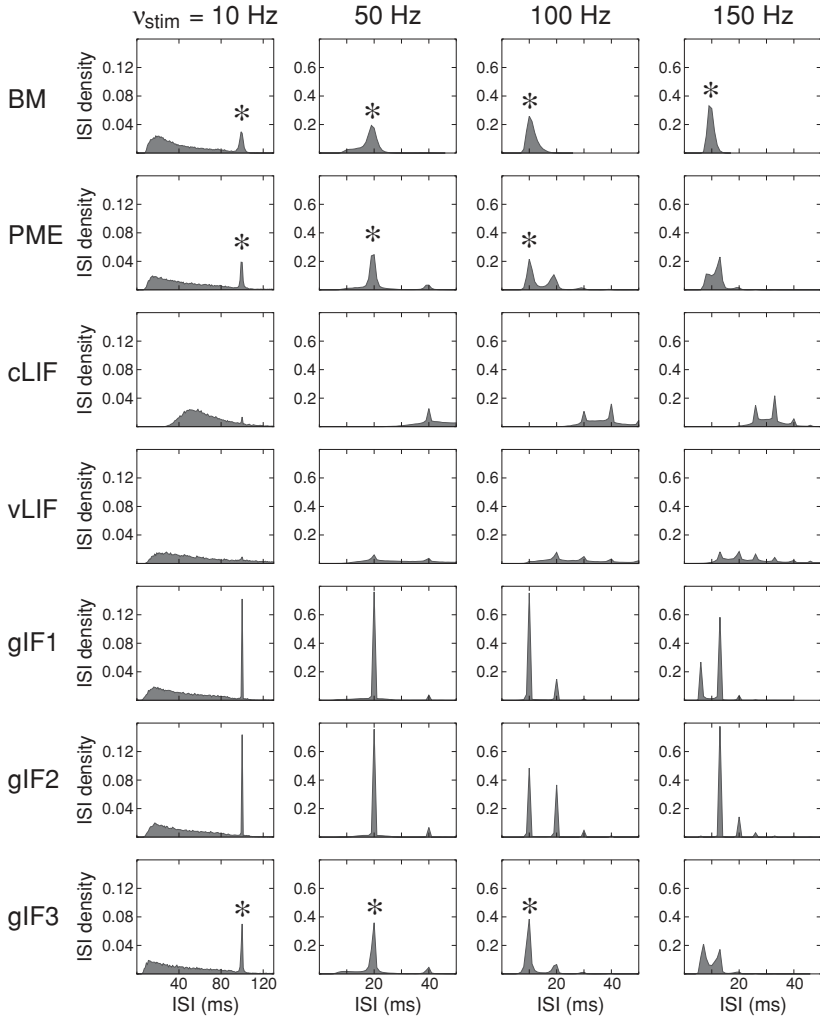
Figure 8: Typical ISIHs for all models at four different stimulation frequencies (10 Hz, 50 Hz, 100 Hz, and 150 Hz; parameters of synaptic inputs are the same as in Figure 7). The cLIF and vLIF model were not able to resolve higher frequencies in a reliable fashion. Together with the gIF1 and gIF2 models, these LIF models showed a locking to the stimulus frequency, thus leading to sudden jumps in the temporal resolution (see Figure 7C). The gIF3 model and passive membrane equation (PME) came closest to the behavior of the biophysical model (BM) with respect to both temporal resolution of high frequencies (see the stars for corresponding modes in the ISIHs) and the lack of locking behavior.

In contrast, the response of the LIF models showed multiple peaks in the ISIH (see Figure 8, cLIF and vLIF) as a result of mode skipping. As in the biophysical model, the ISIs of the peaks decrease for increasing v_{stim}. The latter leads also to a decrease in the amplitude of the leading peak, indicating that fewer and fewer responses can follow the temporal structure of the driving stimulus. For some stimulation frequency and determined by the membrane time constant, this leading peak disappears, and the following peak must be viewed as the direct cellular response to the stimulus. Because the T_{ISI} of the leading peak was used to estimate the temporal resolution (see equation 3.2), this leads to an abrupt change in the temporal resolution, as shown in Figure 7C (left) by the steplike decline. Although the cell still responds locked to the stimulus for higher frequencies, modes of the stimulus are persistently skipped (for a discussion of this issue, see, e.g., Gutkin et al., 2003).

Mode skipping was, although to a smaller extent, also observed in simulations of the passive membrane equation (see Figure 7C, left, PME) as well as the gIF1 and gIF2 model (see Figure 7C). In general, there were fewer modes in the ISIH of the gIF models, indicated by the larger peaks (see Figure 8, gIF1 and gIF2; for the LIF models, many peaks occurred outside the depicted ISI regime shown in Figure 8). Moreover, all gIF models as well as the PME model resolved reliably synaptic inputs beyond 100 Hz frequency. The gIF3 model best reproduced the response behavior found in the biophysical model with respect to both temporal resolution of high stimulating frequencies and a graded decrease of the temporal resolution for very high frequencies (see Figure 7C, right). Quantitative differences observed for the temporal resolution between these two models are primarily attributable to the effects of active membrane conductances, which are significant at high stimulation frequency, as well as the activity-dependent spike threshold present in the biophysical but not the gIF3 model. This conclusion is also supported by the response behavior of the passive membrane with fixed spike threshold, which mimicked that of the biophysical model in both output rate and temporal resolution for a very broad regime at the low end of driving input frequencies (see Figures 7B and 7C, left).

Finally, we note that the ISIHs of the PME and gIF3 models showed in general only one peak (see Figure 8, gIF3 and PME, stars), in accordance with the biophysical model. Only for very large v_{stim} did a second peak occur which, however, was at least for the gIF3 model always less pronounced than the leading peak. These results suggest that not only the sharp firing threshold and, thus, the lack of more realistic spike generation dynamics, can be made responsible for mode skipping, but also the nature of the synaptic inputs. The latter update the membrane state in the LIF model in a state-independent and, thus, current input resembling fashion. This state-independent update is also present in the gIF1 and partially in the gIF2 model, despite the conductance-based dynamics that describes here the cellular behavior in between synaptic inputs.

3.3 Gain Modulation. In a final set of simulations, we addressed the question to which extent the simplified models capture the modulatory effect of synaptic background activity on the response gain. To that end, we stimulated the cells periodically with 0 to 50 simultaneously releasing excitatory synapses with parameter settings given in Table 2, thus leading to synaptic stimuli of different amplitude. In addition, synaptic background activity was altered by scaling the frequency of excitatory and inhibitory inputs between 0.5 and 2.0 around the values given in Table 3. The behavior was then characterized by the probability of emitting a spike in response to a given excitatory stimulus. In all models, the response probability showed a sigmoidal behavior as a function of the stimulation amplitude (see Figure 9). Therefore, the amplitude for which the response probability takes 50% (mid-amplitude) and maximum slope (gain) were used to further quantify the response (see Figure 10A, left).

In all cases, synaptic background activity was efficient in modulating the cellular response (see Figure 9), in particular the response gain. With the exception of the gIF2 model, the response became more graded for increasing frequency of the synaptic background, as indicated by the smaller slope of the response curves for higher synaptic background activity (see Figure 10C). In the LIF models, a sharp decrease of the slope to nearly zero for synaptic background frequencies larger than the one found optimal (see below) was observed (see Figure 10B, left, star). In the gIF2 model (see Figure 9, gIF2), the response probability for a given stimulus amplitude was, in general, higher for smaller synaptic background activity. This result can again be explained by the membrane dynamics of the gIF2 model. In this model, the PSP amplitude depends on the total membrane conductance only and decreases for larger membrane conductance. Therefore, in high-conductance states caused by intense synaptic inputs, the fluctuations of the membrane state variable are reduced, which leads to an effective reduction of the discharge rate and, hence, response probability.

Although the response curves in the different models showed a sigmoidal behavior, only the gIF3 model came qualitatively close to the behavior seen in the biophysical model (see Figure 9; compare BM and gIF3), closely followed by the passive membrane with fixed spike threshold (see Figure 9, PME). In the LIF models, the mid-amplitude covered a huge range of values as a function of the background intensity (see Figure 10B, left, dashed lines). Our results indicate an optimal regime (see Figure 10B, left, star) where the stimulation amplitude is smallest to evoke 50% of the response. This behavior resembles that seen in the stochastic resonance phenomenon; for small noise levels, stronger stimuli are needed to cross firing threshold, whereas more intense synaptic background activity will cause more spontaneous spikes, which interfere with the response to a stimulus with given amplitude.

Although some indications of such an optimal response regime are also present in the biophysical and gIF models (see Figure 10B, right), the
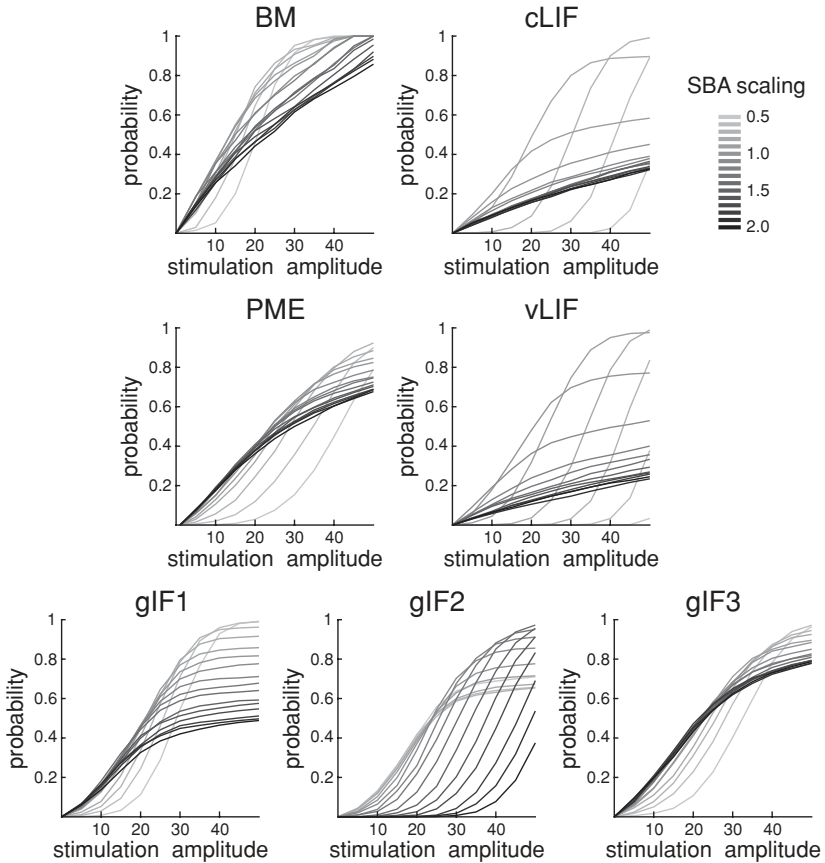
Figure 9: Response probability as function of stimulation amplitude and synaptic background activity for the biophysical model (BM), the passive membrane equation (PME), classic and very leaky IF (cLIF and vLIF, respectively), and the three gIF models (gIF1 to gIF3). The stimulation amplitude is given by the number of simultaneously releasing excitatory synapses (between 0 and 50; see appendix A and Table 2 for parameters). The synaptic background activity was changed by applying a common scaling factor (ranging from 0.5 to 2.0) to the frequency of excitatory and inhibitory synaptic inputs given in Table 3. The response probability shows, in general, a sigmoidal behavior, but only the gIF3 (and to a lesser extend the gIF1) model was able to capture the qualitative behavior of the response curves seen in the biophysical model.

total range of covered mid-amplitudes in these models was much smaller than in the LIF models. This wider working range is a direct result of the conductance-based nature of the given models. The total membrane conductance increases with the level of synaptic activity, this way lowering the
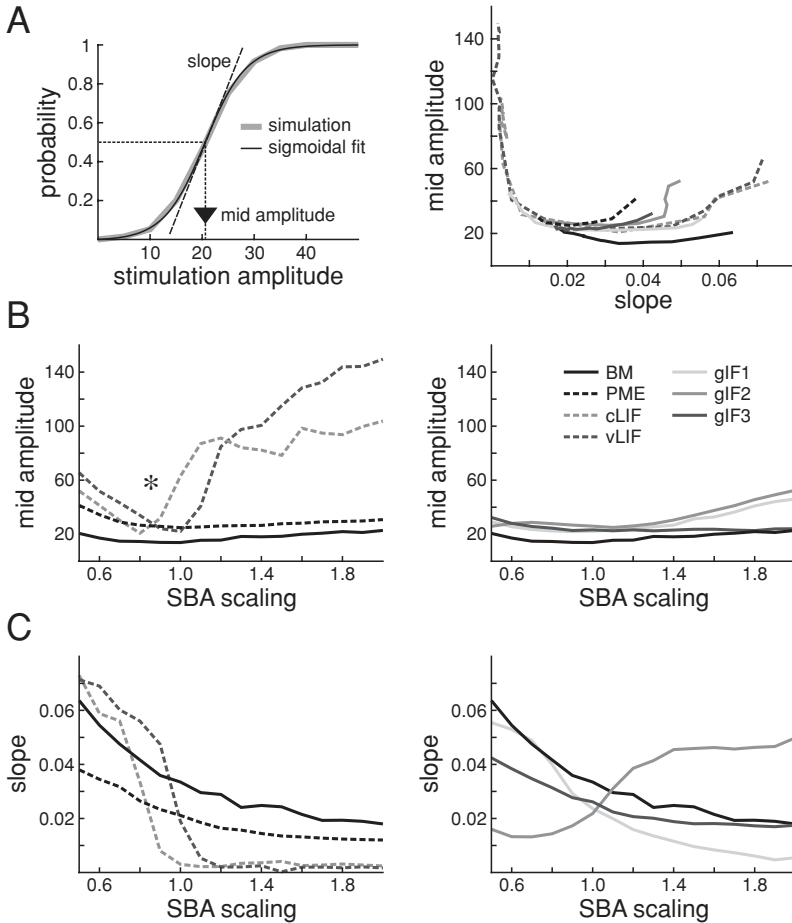
Figure 10: Gain modulation in the biophysical model (BM), the passive membrane equation (PME), classic and very leaky IF (cLIF and vLIF, respectively), and the three gIF models. (A) Left: Response probability $\rho(g_{stim})$ (gray) as a function of the excitatory synapses. $\rho(g_{stim})$ was fit with a sigmoidal function (black) $\rho(g_{stim}) = (1 - \exp(-a g_{stim}))/(1 + b \exp(-a g_{stim}))$, where a and b are free parameters and g_{stim} denotes the stimulation amplitude. From these fits, the stimulation amplitude (number of simultaneously releasing excitatory synapses; see Figure 9) yielding a probability of 50% (mid-amplitude) and the slope were estimated and plotted against each other for different levels of synaptic background activity (right). (B, C) Mid-amplitude and slope of response probability curves as functions of the synaptic background activity (SBA) for the different models. In all cases, the synaptic background activity was changed by applying a common scaling factor (SBA scaling), ranging from 0.5 to 2.0, to the frequency of excitatory and inhibitory synaptic inputs given in Table 3.

probability for evoking a response for stimuli of given amplitude by shifting the response curve to higher-stimulation amplitudes (shunting effect). On the other hand, more intense synaptic activity increases the fluctuation amplitude of the membrane state and thus fosters the (spontaneous) discharge rate. The latter results in a shift of the response curve to smaller stimulation amplitudes. Both effects robustly counterbalance, leaving the mid-amplitude nearly unaffected in the investigated parameter regime. This allows the cell to respond in a discriminating manner over a broad synaptic input regime (see Figures 10B and 10C, solid), which may provide the basis for more efficient computations and therefore add computational advantages to single-cell dynamics. In contrast, in the LIF models, this conductance-induced shift of the response curve is lacking, thus leaving alone the observed increase in the mid-amplitude for increased synaptic noise. This leads to a saturation of the cellular response for moderate total synaptic input rates (see Figures 10B and 10C, dashed) and therefore narrows the synaptic input regime that can be discriminated and utilized for computations.

4 Event-Driven Implementation of gIF Models

The analytic form of the state variable $m(t)$ (see equations 2.14 and 2.24) as well as its update Δm at arrival of a synaptic event (see equations 2.20 and 2.29) allow the introduced gIF models with presynaptic-activity dependent state dynamics to be used together with event-driven simulation strategies. In this section, we first recall briefly the basic ideas behind event-driven and clock-driven simulation strategies, before we present a specific implementation of the proposed models in an event-driven framework along with a coarse evaluation of its performance.

4.1 Clock-Driven vs. Event-Driven Simulation Strategies. In most computational neuronal models, in particular biophysical models, neuronal dynamics is described by systems of, in general, nonlinear coupled differential equations. The strict constraints in solving such systems analytically let to the development of a variety of numerical techniques based on the discretization of space and time. Due to the evaluation of neuronal state variables on a discretized time axis, or time grid, and the fact that times of occurring events, such as synaptic inputs or spikes, are assigned to discrete grid points, such simulation techniques are called *synchronous* or *clock driven*. While the algorithmic complexity, or computational load, scales with the number of neurons in the modeled network as well as the number of differential equations describing the single-neuron dynamics, it also scales linearly with the used temporal resolution or time-grid constant. Although the computational load is expected to be largely independent of the activity in the network, the temporal discretization in numerical methods utilizing in particular fixed-time steps introduces an artificial cutoff for timescales

captured by the simulation. As a direct consequence, short-term dynamical transients might not or only incompletely be captured (Tsodyks et al., 1993; Hansel et al., 1998). Moreover, the artificial assignment of event times to grid points might lead to a bias in dynamic behaviors, such as the emergence of synchronous network activity or oscillating network states (e.g., Hansel et al., 1998; Shelley & Tao, 2001) or to an impact on the weight development of synapses subject to spike-timing dependent plasticity that we have observed.

A more accurate way for simulating neural activity is to keep the exact event times and to evaluate state variables at the times of occurring events, thus setting the algorithmic complexity free from its dependence on the temporal resolution. Such an *asynchronous* or *event-driven* approach was proposed recently (Watts, 1994; Mattia & Del Giudice, 2000; Reutimann et al., 2003). It makes use of two ideas. First, in biological neural networks, interaction between neurons occurs primarily by synaptic interactions, which can be viewed as discrete events in time. Second, at least in mammalian cortex, the average firing rate is low (around 10 Hz for spontaneous activity during active states; see Evarts, 1964; Hubel, 1959; Steriade, 1978; Matsumura, Cope, & Fetz, 1988; Holmes & Woody, 1989; Steriade, Timofeev, & Grenier, 2001). Therefore, synaptic events occur rather isolated, and a single neuron is dynamically decoupled from the network for most of the time. If the differential equations describing the biophysical dynamics allow an analytic solution of the state variables (for a relaxation of this requirement, see Hines & Carnevale, 2004; Lytton & Hines, 2005), the neuronal state at a time t can be explicitly determined from an initial state at an earlier time t_0 and the elapsed time interval $t - t_0$ without iteratively updating state variables at a discrete time step in between t_0 and t. This uncouples the computational load from the numerical accuracy of the simulation and, thus, from constraints imposed on timescales of involved biophysical processes. However, it does so at the expense of the requirement for an analytically describable evolution, either exact or approximated, of the neural state variables. Moreover, although the computational load still depends on the number of neurons in the same way as in clock-driven approaches, it scales now in addition linearly with the number of events, that is, with the average activity, in the network.

However, evaluating the activity-dependent computational load in the event-driven simulations with that of clock-driven simulations with reasonable temporal resolution suggests that the event-driven simulation strategy remains a highly efficient alternative to clock-driven approaches if network activity typically seen in the cortex in vivo is considered. For instance, assuming a network of N neurons each interconnected by 10^4 synapses (Szentagothai, 1965; Cragg, 1967; Gruner, Hirsch, & Sotelo, 1974; DeFelipe & Farĩnas, 1992; DeFelipe, Alonso-Nanclares, & Arellano, 2002) and with an average discharge rate of 10 Hz for each neuron (e.g., Steriade et al., 2001), the total number of events generated is of the order of $N \cdot 10^5$ per second.

This number equals that of state variable updates, which need to be performed within the same time interval. On the other hand, in clock-driven simulations, $N \cdot dt$ state variable updates have to be performed, where dt denotes the temporal resolution of the simulation. Thus, for $dt = 0.01$ ms, the number of state updates is the same in both simulation approaches. However, the event-driven simulation will be superior in accuracy compared to the approach with fixed temporal binning, as the precision is constrained only by the limitations set by the machine precision.

4.2 A Specific Event-Driven Implementation. In its most efficient implementation, an event-driven simulation strategy makes use of an analytic form of the state equations describing the evolution of the membrane state variables in between the arrival of synaptic events. This way, the sole knowledge of the membrane state at the last synaptic event along with the time difference is sufficient to calculate and update the state variables at the arrival time of a new synaptic event. This allows "jumping" from event to event rather than evaluating the membrane state variables on a temporal grid that defines synchronous or clock-driven simulation strategies.

In all IF neuron models with presynaptic-activity dependent state dynamics proposed here (gIF1 in section 2.3, gIF2 in section 2.4, and gIF3 in section 2.5), the equations describing the membrane state and its update at arrival of synaptic events are analytically closed and, hence, applicable in event-driven simulations. We incorporated the gIF models in the NEURON simulation environment (Hines & Carnevale, 1997, 2004), which provides an efficient and flexible framework for event-driven modeling (scripts for the gIF models are available online at http://cns.iaf.cnrs-gif.fr/), as well as a custom C/C++ software tool for large-scale network simulations. In these implementations, the following steps are executed on arrival of a synaptic event at time t_1:

Step 1. At the arrival of a synaptic event, independent of the current state of the membrane, the actual membrane time constant $\tau_m(t_1)$ and its synaptic contributions $\tau_m^{\{e,i\}}(t_1)$ are calculated using equation 2.13 (for gIF1, gIF2, and gIF3) with the values of the synaptic contributions to the membrane time constant $\tau_m^{\{e,i\}}(t_0)$ for the previous synaptic event at time t_0.

Step 2. In the gIF3 model, the effective reversal state $m_{rest}(t_1)$ is calculated (see equation 2.25) based on the value of the synaptic contributions to the membrane time constants $\tau_m^{\{e,i\}}(t_1)$ at time t_1 (calculated in step 1).

Step 3. If the neuron is not in its refractory period, the state variable $m(t_1)$ is calculated using equation 2.14 for the gIF1 and gIF2 models or equation 2.24 for the gIF3, in which t_0 denotes the time of the previous synaptic event, $m(t_0)$ is the membrane state, and $\tau_m^{\{e,i\}}(t_0)$ are the excitatory

and inhibitory synaptic contribution to the total membrane time constant at time t_0. For the gIF3 model, in addition, the actual effective reversal state $m_{rest}(t_1)$ (calculated in step 2) is used.

Step 4.   If the neuron is not in its refractory period, the state variable $m(t_1)$ is updated by $\Delta m_{\{e,i\}} = const$ (for gIF1 model), $\Delta m_{\{e,i\}}(\tau_m(t_1))$ (for gIF2 model, equation 2.20), or $\Delta m_{\{e,i\}}(\tau_m(t_1), m(t_1))$ (for gIF3 model, equation 2.29), where the indices e and i denote excitatory and inhibitory synaptic inputs, respectively.

Step 5.   Depending on the type of synaptic input received at time t_1, the corresponding synaptic contribution to the membrane time constant $\tau_m^{\{e,i\}}(t_1)$ is updated by $\Delta\tau_m^{\{e,i\}} = const$ (see equation 2.16 for gIF1, gIF2 and gIF3).

Step 6.   If the updated $m(t_1)$ exceeds the firing threshold m_{thres}, a spike is generated and the cell enters an absolute refractory period after which the state variable is reset to its resting value m_{rest}. The spike event is added to an internal event list and causes, after a transmission delay, a synaptic event in each target cell.

Note that this implementation constitutes only one possibility, as the order of updating state variables can be modified.

4.3 Performance Evaluation. As outlined in the previous section, the analytic form of the state equations allows the use of the gIF models in precise and efficient simulation strategies—in particular, event-driven simulation approaches. However, due to a more complex dynamics of the gIF models compared to the LIF neuron models, a reduction in performance compared to their LIF counterparts must be expected. To investigate this issue in more detail, we analyzed the performance of all neuron models by comparing the time needed to simulate 100 s of neural activity in the NEURON simulation environment (Hines & Carnevale, 1997, 2004), running on a 3 GHz Dell Precision 350 workstation (see appendix A). In the LIF and gIF models, synaptic inputs were chosen to be Poisson distributed with a rate between 4 and 80 kHz for the excitatory channel and between 1 and 20 kHz for the inhibitory channel. Both rates were varied proportionally, such that the total average rate took values between 5 and 100 kHz. In the biophysical model, 8000 excitatory and 2000 inhibitory channels were driven by Poisson distributed inputs with average rates between 0.5 and 10 Hz, thus yielding the same total average rate. Synaptic and cellular properties were the same as in the previous models (see Tables 1 and 2 as well as appendix A).

In the investigated input parameter regime, the total simulation time, consisting of both the updates of the neural state variables and the

generation of random synaptic inputs, was at least two orders of magnitude smaller for the IF neuron models compared to the biophysical model (see Figure 11A). Moreover, as expected, for lower and biophysically more realistic input rates around 20 kHz, the event-driven simulation strategy was more efficient than the clock-driven simulation approach (see Figure 11A; compare the solid and dashed lines). However, event-driven simulations were at higher rates due to their approximately linear scaling of the simulation time with number of events (note the logarithmic scale in Figures 11A to 11C; for linear plots, see the insets), outperformed by corresponding clock-driven simulations (see Figure 11A, star). The performance of the latter was nearly independent on the input drive.

Considering the time needed for updating the neuronal state variables only, no significant differences between clock-driven and event-driven simulation strategies were observed in the case of the LIF and gIF models (see Figure 11B; compare the gray dashed and solid lines). Whereas the performance of the biophysical model as well passive membrane model with fixed spike threshold remained nearly independent on the input drive (see Figure 11B, black solid and dashed lines), both the LIF and gIF models showed an approximately linear scaling with total input rate (see Figure 11B, gray solid and dashed lines; see also the inset), independent of which simulation strategy was used. This linear scaling behavior with the number of events is expected for event-driven simulation strategies. Its unexpected appearance in clock-driven simulations, where the simulation time depends ideally on only the chosen temporal resolution, can be explained by the use of a common optimization scheme as well as the relation between temporal resolution t_{res} of the simulation and the number of occurring events. Although in the ideal clock-driven approach, the neuronal state is evaluated at each point on a fixed time grid, optimization can be achieved if the state variable is not updated because no synaptic event was present within the preceding time interval of length t_{res}. Thus, the state updates, which constitute the major part of the computational load in the considered models, are mainly driven by input events as long as the number of events (total input rate) is smaller than $1/t_{res}$. This leads to a scaling comparable to that expected for pure event-driven simulation strategies. Accordingly, due to the use of a time resolution of 0.01 ms (see section A.3), for biophysically rather unrealistic rates beyond 100 kHz, the clock-driven simulations no longer scaled with the input rates and therefore ran faster than corresponding event-driven simulations. A better performance for clock-driven simulations was also achieved by lowering the temporal resolution, but not without crucial impact on the precision (for a discussion of this subject, see Hansel et al., 1998; Shelley & Tao, 2001).

Finally, the LIF neuron model outperformed the biophysical model on average by a factor of about 600 and the passive membrane model by a factor of 15, whereas the gIF models were, on average, only a factor of three slower than the corresponding LIF simulations (see Figures 11C and 11D).
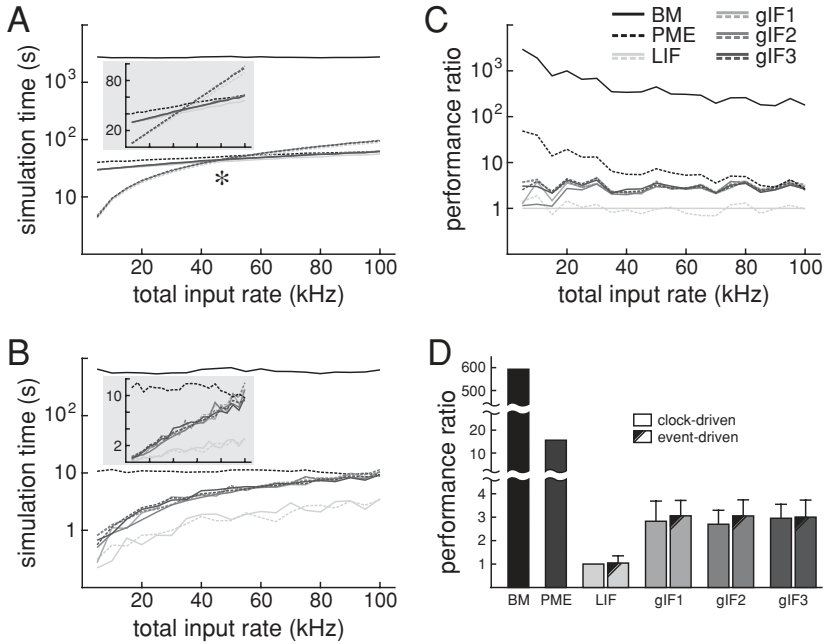
Figure 11: Performance evaluation of the biophysical model (BM), the passive membrane equation (PME), the leaky IF (LIF) as well as the three gIF models (gIF1 to gIF3). (A) Total time needed for simulating 100 s neural activity (neural dynamics and generation of random synaptic inputs) as a function of the total synaptic input rate. Whereas in clock-driven simulations (solid lines) the simulation time was nearly independent of the input rate, a linear scaling with input rate was observed in event-driven simulations (dashed lines; see the linear plot in the inset). The star marks the setting for which the efficacies of clock- and event-driven stimulation approaches change (see text). (B) Total time needed for simulating 100 s neural activity (neural dynamics without generation of random synaptic inputs) as a function of the total synaptic input rate. Both simulation strategies yield the same qualitative scaling behavior, with the gIF models only minimally slower than the LIF neuron model. The inset shows a linear plot of the simulation times for the LIF and gIF models. (C) Performance ratios relative to the clock-driven simulation of the LIF neuron model as a function of total input rate (neural dynamics only; see B). Whereas the gIF models were only about three times slower than the LIF neuron models in the investigated input parameter regime, the biophysical model showed about a 600 times performance deficit, and also the clock-driven simulation of the passive membrane equation (PME) remained about 15 times slower that equivalent simulations with the LIF model. (D) Comparison between the performance, normalized to the clock-driven simulation of the LIF neuron model (BM: 592.8; PME: 15.65; IF, clock driven: 1.04 ± 0.31; gIF1 to gIF3, clock driven: 2.82 ± 0.86, 2.70 ± 0.59, 2.95 ± 0.59; gIF1 to gIF3, event driven: 3.06 ± 0.66, 3.05 ± 0.69, 3.01 ± 0.73).

This performance deficit is a direct consequence of the more complicated neuronal dynamics defining the gIF models. The latter contains the calculation of additional exponentials, which constitute the main computational load in the implementation. Without major impairment of precision, this load can be dramatically reduced by the use of look-up tables as well as the reduction of memory and function call overheads by optimized C/C++ programming. Preliminary results using an event-driven implementation of the classic IF model in custom C/C++ software show that 100 million events could be simulated in less than 90 s using a standard PC-based workstation (see appendix A). From these, about 97.8% (approximately 88 s) account for the generation of random synaptic inputs as described above, and 2.2% (approximately 2 s) for the update of the neural state variable of the IF model. This compares to about 860 s and 70 s for generating random synaptic inputs and updating neural state variables in the classical IF neuron model, respectively, if the same number of events is handled in the NEURON simulation environment, thus indicating a further performance gain of at least one order of magnitude with customized C/C++ implementations. The latter would allow simulating in real time medium-scale neural networks of a few thousand neurons with biophysically more realistic conductance-based dynamics and average rates of a few Hz.

5 Discussion

The leaky integrate-and-fire neuron model, whose dynamics is characterized by an instantaneous change of the membrane state variable upon arrival of a synaptic input, followed by a decay with fixed time constant, has proven to be an efficient model suitable for large-scale network simulations. However, due to its simple dynamics, in particular, the current-based handling of synaptic inputs, the use of the LIF model for simulating biophysically more realistic neural network behavior is strongly limited. In this article, we proposed a simple extension of the LIF neuron toward conductance-based dynamics, the gIF model, which is consistent with the impact of synaptic inputs under in vivo–like conditions. Below we summarize and discuss the basic approach we followed here, along with an evaluation of the performance and possible extensions of the proposed gIF models with conductance-based state dynamics.

5.1 The gIF Neuron Models. With respect to their dynamical complexity, gIF models are situated in between the LIF and full conductance-based IF models, which were modeled here by a passive membrane equation with fixed spike threshold. Whereas the membrane state still undergoes an instantaneous change upon arrival of a synaptic input, the following decay is governed by a time-dependent membrane time constant whose value is the result of synaptic activity. This state-dependent dynamics captures the primary effect of synaptic conductances on the cellular membrane and

therefore describes a simple implementation of time-varying conductance states, as found in cortical neurons during active network states in vivo.

Extensions of the model investigated in this article include the incorporation of the scaling of postsynaptic potentials as a function of the total membrane conductance (gIF2 model) as well as take into account changes in the driving force due to the presence of synaptic reversal potentials (gIF3 model). As we have shown, in all cases, the state-dependent membrane state dynamics of the gIF models is described by simple analytic expressions, thus providing the basis for an implementation of these models in exact event-driven simulation strategies. The latter have proven to be an efficient alternative to the most commonly used clock-driven approaches for modeling medium- and large-scale neural networks with biophysically realistic activity.

5.2 Response Characteristics of gIF Neuron Models. To test the validity of the proposed models, the spiking response behavior was compared with that of LIF neurons, a model of a passive membrane with exponential synapses and fixed spike threshold, as well as of a biophysically detailed model of cortical neurons with Hodgkin-Huxley spike-generation mechanism and two-state kinetic synapses. Three aspects of neural dynamics were investigated. First, the statistical investigation of the spontaneous discharge activity with respect to firing rate and irregularity for corresponding synaptic input parameters showed that, compared to the LIF models, the gIF1 and gIF3 models reproduced much better the behavior seen in the biophysical model. Second, due to the explicit incorporation of presynaptic-activity dependent state dynamics, only the gIF1 and gIF3 models showed a temporal resolution of synaptic inputs, which was comparable to that seen in the more realistic biophysical model. Finally, due to the synaptic input-dependent dynamics of the gIF models, aspects of gain modulation seen in the biophysical model were much better captured by the gIF1 and gIF3 models than in corresponding LIF neuron models. Interestingly, despite its mathematically simpler structure, the response behavior of the gIF3 model came generally closer to the biophysical model, as compared to the PME model. This marked gain in a more realistic biophysical dynamics capturing faithfully crucial aspects of high-conductance states in vivo was a trade-off, with only a minor decrease in computational performance compared to the LIF neuron model.

The gIF2 model, however, failed to qualitatively and quantitatively reproduce the response behavior seen in the gIF1 and gIF3 models, as well as the biophysical model. Recalling its definition, the cellular dynamics of this intermediate model captures only the impact of the actual total membrane conductance, or membrane time constant, on the amplitude of PSPs, but not their dependence on the actual membrane state and, hence, distance to corresponding synaptic reversal potentials. The reported observations therefore suggest that both the total membrane conductance and

membrane state dependent scaling of the postsynaptic potentials are crucial
to recover a more realistic conductance-driven neuronal state dynamics.

5.3 Limits of the gIF and LIF Neuron Models. An overall evaluation of
response characteristics of the gIF models, in particular the gIF3 model, in
comparison with those of the LIF neuron models suggests that the former
provide a better description of neural dynamics observed in the detailed
biophysical model or real cells. However, the simple analytic description
of these models also strictly limits the dynamic behaviors which can be
faithfully reproduced. As our simulations show, the most notable quantita-
tive differences between the gIF3 and biophysical model are found in the
spontaneous discharge activity (see Figure 4). Although the general depen-
dence of the output rate ν_{out} on the excitatory and inhibitory input rates is
reproduced, the firing rates in the gIF3 model cover a much broader regime
than in the biophysical model, especially at higher input rates. The primary
reason for this difference is the missing description of conductance-based
spike-generating mechanisms, which, especially at high firing rates, will
lead to an additional contribution to the total membrane conductance and
modulate the shunting properties of the membrane and shape the response
to the driving synaptic inputs. This conclusion was confirmed by using a
purely passive model with a fixed threshold mechanism replacing a more
realistic spike generation. Surprisingly, the deviations from the biophysical
model were stronger than in the gIF3 model, probably due to the difference
in handling the update of the membrane state upon arrival of a synaptic
input. Indeed, this observation suggests that the instantaneous update of
the membrane state could effectively mimic the fast transient changes of
membrane conductance and time constant caused by the activation of spike-
generating conductances. However, despite the excellent match between
the gIF3 and biophysical model, the deviations at high input and firing
rates resulting from the additional effect of active membrane conductances
constitute one crucial limit of the gIF models. On the other hand, the LIF
neuron models incorporate neither of these activity-dependent shunting ef-
fects and must, in this respect, be considered a less faithful approximation
of biophysical neuronal dynamics.

The fixed threshold description of spike generation in the gIF models will
also have an impact on the achievable variability of spontaneous responses.
Although the gIF3 model came qualitatively closest to reproducing the in-
put dependence of the spontaneous discharge variability (see Figure 5), the
C_V was in general lower than in the biophysical model, although well in the
experimentally observed regime (e.g., see Rudolph & Destexhe, 2003). This
indicates that the lack of faithful description of spike generation might set
another crucial limit in the dynamic behaviors that can be captured by the
gIF models or any other passive model with fixed spike threshold. Specifi-
cally, a variable spike threshold and fast transient changes in the membrane
conductance linked to spike generation provide other sources of variability

in the neuronal discharge in conjuction with the synaptic input drive. Indeed, the upper limit of achievable C_V values in the gIF model, as in the PME model, is defined by the synaptic inputs (for independent Poisson inputs $C_V \leq 1$), whereas active membrane conductances linked to spike generation can lead to a $C_V \gg 1$, for example, in bursting cells (Svirskis & Rinzel, 2000). Fusing simple IF neuronal models incorporating biophysically more realistic membrane dynamics (e.g., Lytton & Stewart, in press) with the idea behind the gIF models could provide a way for reproducing the full diversity of irregular discharge behaviors seen experimentally. In the classical LIF model considered here, the limiting factors are the fixed spike threshold and current-based description of synaptic activity, which were shown to yield generally lower C_V values (e.g., Rudolph & Destexhe, 2003).

Finally, other quantitative differences between the gIF3 model and the biophysical model were observed, such as the enhanced temporal resolution for input frequencies above 100 Hz (see Figure 7C) or the shallower scaling of the response gain as a function of overall synaptic activity (see Figure 10) in the gIF3 model. These differences can be traced back to the absence of a biophysically realistic spike-generating mechanism, although these can be incorporated (see below). However, the observed differences between the gIF, in particular the gIF3, and biophysical models were less crucial than between the biophysical and the passive model with fixed spike threshold, despite the fact that the latter reproduced realistic PSP shapes and thus should capture temporal aspects of membrane dynamics to a better extent. Much more crucial were the differences observed between the biophysical model and the LIF model, in which both spike-generating mechanisms as well as conductance-based synaptic activity are absent. In this case, not just quantitative differences in the investigated response behavior were observed, but qualitative differences such as a sensitive scaling of the spontaneous discharge, which is responsible for the narrow regime where highly irregular activity can be observed (see Figure 5) or the failure to faithfully resolve high-frequency synaptic inputs (see Figure 7). The missing activity-dependent membrane dynamics also results in a modulation of response gain that markedly deviates from those observed in real cells (see Figure 10; e.g., Chance et al., 2002; Fellous, Rudolph, Destexhe, & Sejnowski, 2003; Prescott & De Koninck, 2003; Shu, Hasenstaub, Badoual, Bal, & McCormick, 2003).

5.4 Possible Extensions of gIF Neuron Models. The proposed simple extensions of the LIF model concern only synaptic inputs. Neither active membrane conductances, such as those considered in the spike response model (e.g., Gerstner & van Hemmen, 1992, 1993; Gerstner et al., 1993; Gerstner & Kistler, 2002), nor simplifications of spike-generation mechanism (e.g., based on Hodgkin-Huxley kinetic models; Hodgkin & Huxley, 1952), such as those considered in the various instances of nonlinear

IF neuron models (e.g., Abbott & van Vreeswijk, 1993; Fourcaud-Trocmé et al., 2003; for a general review, see Gerstner & Kistler, 2002), were incorporated into the gIF models. The gIF models presented here are also different from mathematically more abstract models (e.g., Izhikevich, 2001, 2003) and will not capture intrinsic phenomena like bursting or spike rate adaptation. Moreover, the instantaneous update of the membrane state variable upon arrival of a synaptic input abstracts from a more realistic shape of the membrane potential following synaptic stimulation (for a model that considers this aspect, see, e.g., Kuhn, Aertsen, & Rotter, 2004). Therefore, aspects of neuronal dynamics that depend on both the exact form of PSPs or the presence of intrinsic state-dependent membrane currents cannot be captured by the gIF models proposed here.

However, as we show, a great variety of principal spiking response characteristics for both spontaneous and stimulated synaptic activity can be faithfully described by models incorporating a synaptically driven fluctuating membrane time constant, that is, a presynaptic-activity dependent state membrane dynamics, alone. This includes spontaneous activity typically seen in high-conductance states in cortical networks in vivo, as well as the response to transient synaptic stimuli occurring during such states. We suggest that this crucial but restricted gain in realistic biophysical dynamics capturing characterizing aspects of high-conductance states in vivo is a fair trade for the simplicity of the considered extensions, which allow the efficient application in large-scale network models.

Various extensions of the gIF model are currently under investigation (see also appendix C). First, the gIF1 to gIF3 models do not incorporate realistic PSP time courses, but instead are described by an instantaneous update of the membrane state upon arrival of a synaptic input. To relax this restriction and approach biophysically more realistic situations, analytic approximations of the full solution of the membrane equation can be used. A first attempt in this direction is presented in section C.1 for the PSPs of a passive leaky membrane subject to synaptic inputs with exponential conductance time course. The obtained approximation (gIF4 model; see equation C.4) describes excitatory and inhibitory postsynaptic potentials to an excellent extent (see Figures 12A to 12C). Moreover, the mathematical form of this approximation is sufficiently simple to allow implementation of the resulting model in the framework of the event-driven simulation strategy. However, for this purpose, the latter needs to be modified by incorporating the prediction of threshold crossings to scope with responses that, due to the PSP time course, occur now temporally separated from the synaptic input (see Figure 12D).

Second, the gIF1 to gIF3 models do not incorporate spike-generating mechanisms but instead are based on purely passive membrane dynamics. To relax this restriction, simplified models describing active membrane conductances need to be considered. First attempts in this direction are presented in sections C.2 and C.3, where the quadratic IF (Latham,

Richmond, Nelson, & Nirenberg, 2000; Feng, 2001; Hansel & Mato, 2001; Brunel & Latham, 2003; Fourcaud-Trocmé et al., 2003) and the exponential IF (Fourcaud-Trocmé et al., 2003) neuron models, respectively, are extended within the context of the gIF model approach. Although in all cases considered so far, the defining state equation cannot be solved analytically, appropriate approximations of their solutions might provide a sufficiently exact and mathematically simple description of active membrane dynamics close to spike threshold. With such descriptions, the modified event-driven simulation strategy mentioned above can be utilized to implement the resulting models for efficient and precise network simulations. This approach might also be extendable to linearized versions of active membrane currents described by Hodgkin-Huxley kinetics (e.g., Mauro, Conti, Dodge, & Schor, 1970; Koch, 1999) and yield analytically simple expressions for the membrane state equations, thus allowing the capture of aspects of subthreshold activity of active conductances in a computationally efficient way.

Third, the gIF1 to gIF3 models do not incorporate specific intrinsic cellular properties, such as adaptation or bursting. However, the fact that the passive membrane equation B.1 can still be solved analytically in the presence of an exponentially decaying function coupled to a linear function of the membrane state variable allows modeling biophysically more realistic membrane dynamics in an exact and efficient way (e.g., Lytton & Stewart, in press).

Fourth, so far the emergence of high-conductance states requires an intense synaptic activity modeled by individual synaptic input channels. Although this is assumed to occur naturally in large-scale neural networks with self-sustained activity, this requirement might not be fulfilled in smaller network models or sparsely connected networks. The gIF models could be extended by including effective noise sources, as proposed by Reutimann et al. (2003) in the context of event-driven simulation strategies.

Finally, the gIF1 to gIF3 models incorporate synaptic dynamics described by an exponential conductance time course. To relax this restriction, neuronal dynamics can be extended to other and more realistic synaptic kinetic models, such as conductance changes following α-functions (Rall, 1967), n-state kinetics (Destexhe et al., 1994, 1998; Destexhe & Rudolph, 2004), or a frequency-dependent dynamics (e.g., Lytton, 1996; Markram et al., 1998; Giugliano, 2000). The availability of exact event times in event-driven simulation approaches also allows the straightforward implementation of spike-timing dependent plastic changes (e.g., according to models in Song & Abbott, 2001; Froemke & Dan, 2002).

5.5 Future Directions. In addition to the different extensions of the gIF models outlined in the previous section, possible future research directions also include a more detailed study of each model with respect to specific dynamic behaviors. So far, only basic response characteristics, such

as the spontaneous discharge (see section 3.1) or the response to periodic synaptic drive (see sections 3.2 and 3.3), were investigated. Other response characteristics, such as the cellular response to oscillating input currents in high-conductance states, in particular the frequency-response behavior (Brunel, Chance, Fourcaud, & Abbott, 2001; Fourcaud-Trocmé et al., 2003) and instantaneous spike frequency (Rauch, La Camera, Lüscher, Senn, & Fusi, 2003), or the detection of brief transient changes in statistical properties of the synaptic inputs, such as the temporal correlation among the activity of individual input channels (Rudolph & Destexhe, 2001), could provide further insight into the validity and limitations of the proposed simplified neuron models. Furthermore, differences in behaviors seen among these models, in particular between current-based and conductance-based models, will reveal basic requirements that neuronal models have to fulfill in order to reproduce specific dynamic behaviors faithfully. The latter could be used to constrain the complexity of neuronal models used in large-scale network simulations, thus allowing the construction of more efficient network models.

Another important aspect linked to the faithful reproduction of specific and biophysically realistic neuronal behaviors using simplified models is the correct choice of model parameters. In this article, the subthreshold dynamics, specifically the characteristics of synaptic inputs as well as

---

Figure 12: A gIF model with realistic PSP time course. (A) Comparison of excitatory (top) and inhibitory (bottom) postsynaptic potentials in the gIF4 model (black traces; equation C.2) and the LIFcd model (gray traces; numerical solution of equation B.1). Traces are shown for different membrane potentials ranging from the leak reversal E_L to the firing threshold E_{thres}, as well as for three different total membrane conductances given in multiples of the leak conductance G_L ($G_L = 17.18$ nS). Used model parameters for the simulations are given in Tables 1 and 2. (B) Relative error $(V_{LIFcd}(t) - V_{gIF4}(t))/(V_{LIFcd}(t) - E_{thres})$ between the numerical solution of the PSP time course in the LIFcd model ($V_{LIFcd}(t)$) and the gIF4 model ($V_{gIF4}(t)$) at firing threshold as a function of time after synaptic input. Results are shown for the three total membrane conductances used in A. In all cases, the error was smaller than 1% for times covering the PSP peak (gray area), suggesting the possibility of precise prediction of spike times based on the simple analytic state equation describing the gIF4 model (equation C.4). (C) Example of a membrane potential time course resulting from a barrage of synaptic inputs. The numerical solution of the LIFcd model (gray) is compared with the gIF4 model (black) for identical synaptic input pattern (total input rate 100 Hz). (D) Generalization of the event-driven simulation strategy. Upon arrival of a synaptic event at time t, the membrane state (black) is updated from its value at t_0. Threshold crossing is predicted (t_s) and overwritten (t'_s) if another synaptic event arrives at $t_1 < t_s$.
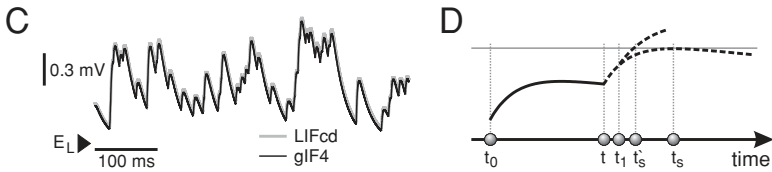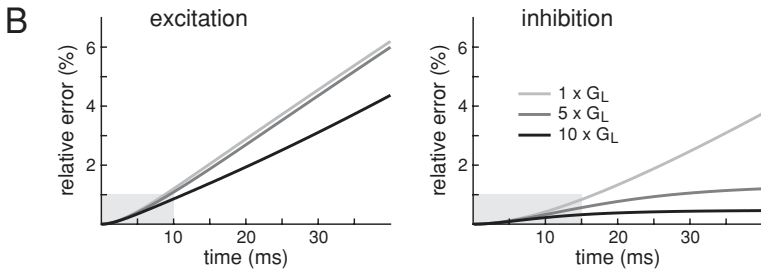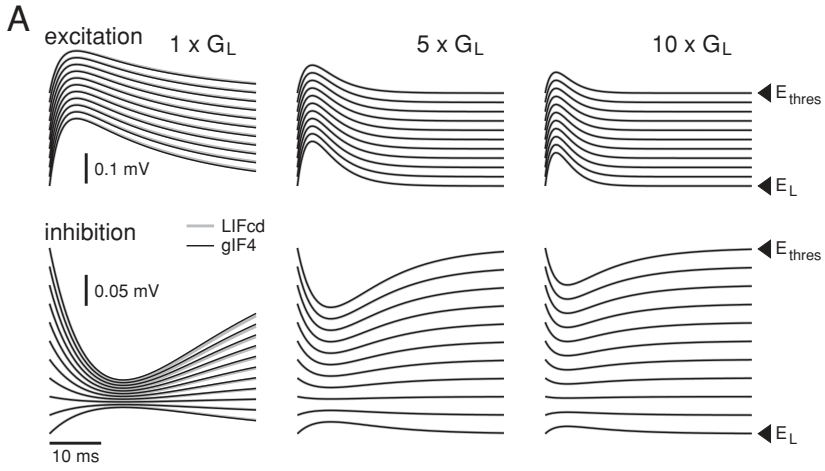
postsynaptic potentials, of a biophysically detailed model were used to adjust parameters in the simpler LIF and gIF models. Other studies used suprathreshold response characteristics, such as the output firing rate (e.g., Rauch et al., 2003) or static as well as the dynamic response properties (Fourcaud-Trocmé et al., 2003), to fit model parameters in conductance-driven and current-driven LIF models. In further investigations, techniques for fitting high-dimensional parameter spaces, typical for detailed biophysical models and experimental recordings, to low-dimensional ones, must be evaluated with respect to their applicability and quality.

Finally, the most challenging task for the future is to evaluate and understand neuronal dynamics at the network level, in particular under in vivo–like conditions, as well as the emergence of specific functional neuronal behaviors if neuronal models are endowed with self-organizing capabilities, such as plastic synapses. We hope that the simplified models proposed in this article will provide useful and efficient tools to facilitate this task. The evaluation of this method from experimental data and the assessment of its sensitivity at the network level will be the subject of forthcoming studies.

Appendix A: Computational Models and Methods

In this appendix, we briefly describe the biophysical model (BM; section A.1), the IF model based on the passive membrane equation and fixed threshold for spike generation (PME; section A.2), and the various IF neuron models (cLIF, cLIF, gIF; section A.3), and summarize the parameters used for numerical simulations.

A.1 Biophysical Model. In what we refer to as the *biophysical model* (*BM*), membrane dynamics was simulated using a single-compartment neuron, described by the active membrane equation,

$$\frac{dV(t)}{dt} = -\frac{1}{\tau_m^L}\left(V(t) - E_L\right) - \frac{1}{C}\,I_{act}(t) - \frac{1}{C}\,I_{syn}(t)\,. \tag{A.1}$$

Here, $V(t)$ denotes the membrane potential, $E_L = -80$ mV the leak reversal potential, $\tau_m^L = C/G_L$ the membrane time constant, $C = aC_m$ the membrane capacity (specific membrane capacity $C_m = 1\,\mu\text{F cm}^{-2}$, membrane area $a = 38,013\,\mu\text{m}$) and $G_L = ag_L$ the passive (leak) conductance (leak conductance density $g_L = 0.0452\,\text{ms cm}^{-2}$).

In equation A.1, $I_{act}(t)$ denotes the active current responsible for spike generation. Voltage-dependent conductances were described by Hodgkin-Huxley type models (Hodgkin & Huxley, 1952), with kinetics taken from a model of hippocampal pyramidal cells (Traub & Miles, 1991) and adjusted to match voltage-clamp data of cortical pyramidal cells (Huguenard, Hamill, & Prince, 1988). Models for sodium current I_{Na} and delayed-rectifier

potassium current I_{Kd} were incorporated into the model, with conductance densities of 36.1 ms cm^{-2} and 7 ms cm^{-2}, respectively.

The synaptic input current,

$$I_{syn}(t) = G_e^{2s}(t)(V(t) - E_e) + G_i^{2s}(t)(V(t) - E_i), \qquad (A.2)$$

was described by a sum over a large number of individual excitatory and inhibitory synaptic conductances,

$$G_{\{e,i\}}^{2s}(t) = \sum_{n=1}^{N_{\{e,i\}}} \overline{G}_{\{e,i\}}\, m_{\{e,i\}}^{(n)}(t) \qquad (A.3)$$

(see also Table 1) with respective reversal potentials $E_e = 0$ mV and $E_i = -75$ mV. In the last equation, $N_e = 10{,}000$ and $N_i = 3000$ denote the total number of excitatory and inhibitory synapses, modeled by α-amino-3-hydroxy-5-methyl-4-isoxazolepropionic (AMPA) and γ-aminobutyric acid (GABA$_A$) postsynaptic receptors with quantal conductances $\overline{G}_e = 1.2$ nS and $\overline{G}_i = 0.6$ nS, respectively (Destexhe et al., 1994). The functions $m_e^{(n)}(t)$ and $m_i^{(n)}(t)$ represent the fractions of postsynaptic receptors in the open state at each individual synapse and were described by the following pulse-based two-state kinetic equation,

$$\frac{dm_{\{e,i\}}(t)}{dt} = \alpha_{\{e,i\}}\, T(t - t_0)\left(1 - m_{\{e,i\}}(t)\right) - \beta_{\{e,i\}}\, m_{\{e,i\}}(t), \qquad (A.4)$$

for $t \geq t_0$, where t_0 denotes the release times at the synapse in question, $\alpha_{\{e,i\}}$ and $\beta_{\{e,i\}}$ are forward and backward rate constants for opening of the excitatory and inhibitory receptors, respectively. $T(t)$ denotes the concentration of released neurotransmitter in the synaptic cleft at time t and is considered to be a step function with $T(t) = T_{\max}$ for a short time period $t_0 \leq t < t_{dur}$ after a release and $T(t) = 0$ afterward (pulse kinetics). The parameters of these kinetic models of synaptic currents were obtained by fitting the model to postsynaptic currents recorded experimentally (Destexhe et al., 1998), and are given in Table 1.

To simulate synaptic background activity, all synapses were activated randomly according to independent (temporally uncorrelated) Poisson processes with mean rates ν_e and ν_i between 0 and 10 Hz for both AMPA and GABA synapses, respectively. This yielded total input rates from $\nu_e = 0$ to 100 kHz for excitation and from $\nu_i = 0$ to 30 kHz for inhibition.

In some simulations, in particular for evaluating the state dependence of the shape and amplitude of excitatory and inhibitory postsynaptic potentials, synaptic models with exponential conductance time course

$$
G_{\{e,i\}}^{\exp}(t) = \begin{cases} 0 & \text{for } t < t_0 \\ \overline{G}_{\{e,i\}} \exp\left[-\frac{t-t_0}{\tau_{\{e,i\}}}\right] & \text{for } t \geq t_0 \end{cases} \tag{A.5}
$$

or α-kinetics

$$
G_{\{e,i\}}^{\alpha}(t) = \begin{cases} 0 & \text{for } t < t_0 \\ \overline{G}_{\{e,i\}} \frac{t-t_0}{\tau_{\{e,i\}}} \exp\left[-\frac{t-t_0}{\tau_{\{e,i\}}}\right] & \text{for } t \geq t_0 \end{cases} \tag{A.6}
$$

were used. Here, $\overline{G}_{\{e,i\}}$ and $\tau_{\{e,i\}}$ denote quantal conductances and synaptic time constants for excitation and inhibition, respectively. Corresponding parameter values are given in Table 1.

Simulations of 100 to 1,000 s neural activity with a temporal resolution of 0.1 ms were performed using the NEURON simulation environment (Hines & Carnevale, 1997), running on a 3 GHz Dell Precision 350 workstation (Dell Computer Corporation, Round Rock, TX) under the SUSE 8.1 LINUX operating system.

A.2 Passive Membrane Equation with Fixed Spike Threshold. In what we refer to as the *passive membrane equation with fixed spike threshold* (PME), membrane dynamics was simulated using a single-compartment neuron, described by the passive membrane equation,

$$
\frac{dV(t)}{dt} = -\frac{1}{\tau_m^L}\left(V(t) - E_L\right) - \frac{1}{C} I_{syn}(t), \tag{A.7}
$$

with parameter values and synaptic activity described in section A.1. Spike generation was described by a fixed voltage threshold ($E_{thres} = -50$ mV) and reset potential ($E_{rest} = -80$ mV).

Simulations of 1000 s neural activity with a temporal resolution of 0.01 ms were performed using the NEURON simulation environment (Hines & Carnevale, 1997), running on a 3 GHz Dell Precision 350 workstation (Dell Computer Corporation, Round Rock, TX) under the SUSE 8.1 LINUX operating system.

A.3 IF Neuron Models. Integrate-and-fire (IF) neuron models were modeled according to the state equations given in section 2.1 for the classical and very leaky integrate-and-fire neuron models (cLIF and vLIF, respectively), as well as sections 2.3, 2.4, and 2.5 for the gIF1, gIF2, and gIF3

neuron models, respectively. Membrane properties as well as parameter values for excitatory and inhibitory synaptic inputs (see Table 2) were chosen by a normalization of the IF models between the resting state ($m_{rest} = 0$ corresponding to $V_m = E_L = -80$ mV) and the firing threshold ($m_{thres} = 1$, corresponding to $V_m = -50$ mV). Average EPSP and IPSP peak amplitudes were estimated by numerical simulations of the passive membrane equation with synaptic models described by two-state kinetics (see section A.1), and were found to be 0.28 mV for EPSPs and -0.21 mV for IPSPs at firing threshold (used for estimating Δm in the cLIF, vLIF, gIF1, and gIF2 models; see sections 2.1, 2.3, and 2.4, respectively) as well as 0.46 mV (EPSPs) and 0.043 mV (IPSPs) at rest (used for estimating Δm in gIF3 model; see section 2.5).

Synaptic inputs in the gIF models were simulated by exponential conductance changes (see equation A.5) with parameter values given in Table 2. Due to the additivity of synaptic inputs for this case, in all IF models, synaptic inputs were simulated by single independent input channels for excitation and inhibition, with total rates of $0 \leq \nu_e \leq 100$ kHz and $0 \leq \nu_i \leq 30$ kHz, respectively. These rates correspond to those used in the biophysical model (see section A.1). In conjunction with the cLIF neuron model, an additional model with small static membrane time constant (the vLIF model) was considered to mimic high-conductance states with a static synaptic conductance. In this case, synaptic rates were $0 \leq \nu_e \leq 20$ kHz and $0 \leq \nu_i \leq 6$ kHz, respectively. The refractory period in all cases was $t_{ref} = 1$ ms.

To evaluate the computational performance of the constructed models, simulations utilizing the clock-driven simulation strategy (time resolution 0.01 ms) as well as the event-driven simulation strategy (Watts, 1994; Mattia & Del Giudice, 2000; Reutimann et al., 2003) were used. In all cases, simulations of 1000 s neural activity were performed.

Appendix B: The Membrane Equation with Exponential Synaptic Conductance Time Course

In section B.1, we briefly outline the explicit solution of the membrane equation,

$$\frac{dV(t)}{dt} = -\frac{1}{\tau_m^L} (V(t) - E_L) - \frac{1}{C} G_s^{\exp}(t) (V(t) - E_s), \qquad (B.1)$$

for a single synaptic input event arriving at time t_0 and described by an exponential conductance time course:

$$G_s^{\exp}(t) = \begin{cases} 0 & \text{for } t < t_0 \\ \overline{G}\, e^{-\frac{t-t_0}{\tau_s}} & \text{for } t \geq t_0. \end{cases} \qquad (B.2)$$

In equation B.1, E_L and E_s denote the leak and synaptic reversal potentials, respectively. $\overline{G}$ in equation B.2 denotes the maximal conductance linked to the update of the membrane time constant τ_m at time t_0 by $\Delta\tau_m^s = C/\overline{G}$ (see equations 2.6 and 2.7). In sections B.2 and B.3, this solution is then approximated, and simple analytic expressions for the PSP peak amplitude as a function of the actual membrane state under incorporation of the effect of synaptic reversal potential are deduced. These expressions constitute the basis for describing the membrane updates upon arrival of a synaptic input in the gIF2 and gIF3 models and are applicable in event-driven simulation strategies due to their analytic form.

B.1 Solution of the Membrane Equation. To simplify notation but without restriction of generality, we solve equations B.1 and B.2 for $t_0 = 0$. With the boundary condition $V(t)|_{t \to -\infty} \longrightarrow E_L$, equation B.1 yields $V(t) = E_L$ for $t < 0$. For $t \geq 0$, explicit integration gives

$$
V(t) = \exp\left[-\frac{t}{\tau_m^L} + \frac{\tau_s}{\Delta\tau_m^s}\, e^{-\frac{t}{\tau_s}} \right]
$$

$$
\times \left\{ E_L e^{-\frac{\tau_s}{\Delta\tau_m^s}} + \int_0^t ds\, \exp\left[-\frac{s}{\tau_s} + \frac{s}{\tau_m^L} - \frac{\tau_s}{\Delta\tau_m^s}\, e^{-\frac{s}{\tau_s}} \right] \right.
$$

$$
\left. \times \left(\frac{E_s}{\Delta\tau_m^s} + \frac{E_L}{\tau_m^L}\, e^{\frac{s}{\tau_s}} \right) \right\}.
\tag{B.3}
$$

The integral expression, which is of general form

$$
X(t) := \int_0^t ds\, \exp\left[A_1 e^{-\frac{s}{\tau_s}} \right] \left\{ A_2 e^{A_3 s} + A_4 e^{A_5 s} \right\}
$$

with

$$
A_1 = -\frac{\tau_s}{\Delta\tau_m^s}, \qquad A_2 = \frac{E_s}{\Delta\tau_m^s}, \qquad A_3 = -\frac{1}{\tau_s} + \frac{1}{\tau_m^L},
$$

$$
A_4 = \frac{E_L}{\tau_m^L}, \qquad A_5 = \frac{1}{\tau_m^L},
$$

can be rewritten in terms of gamma functions. To that end, we expand the factor $\exp[A_1 e^{-t/\tau_s}]$:

$$
X(t) = \sum_{n=0}^{\infty} \int_0^t ds\, \frac{A_1^n}{n!}\, e^{-\frac{s}{\tau_s} n} \left\{ A_2 e^{A_3 s} + A_4 e^{A_5 s} \right\}
$$

$$
= \sum_{n=0}^{\infty} \int_0^t ds\, \frac{A_1^n}{n!} \left\{ A_2 e^{-\frac{n - A_3 \tau_s}{\tau_s} s} + A_4 e^{-\frac{n - A_5 \tau_s}{\tau_s} s} \right\}
$$

$$= \sum_{n=0}^{\infty} \frac{A_1^n}{n!} \left\{ \frac{A_2 \tau_s}{A_3 \tau_s - n} \left(e^{-\frac{n - A_3 \tau_s}{\tau_s} t} - 1 \right) + \frac{A_4 \tau_s}{A_5 \tau_s - n} \left(e^{-\frac{n - A_5 \tau_s}{\tau_s} t} - 1 \right) \right\}$$

$$= A_2 \tau_s (-A_1)^{A_3 \tau_s} \left\{ \Gamma[-A_3 \tau_s, -A_1 e^{-\frac{t}{\tau_s}}] - \Gamma[-A_3 \tau_s, -A_1] \right\}$$

$$+ A_4 \tau_s (-A_1)^{A_5 \tau_s} \left\{ \Gamma[-A_5 \tau_s, -A_1 e^{-\frac{t}{\tau_s}}] - \Gamma[-A_5 \tau_s, -A_1] \right\},$$

where the incomplete gamma function $\Gamma[z, a] = \int_a^{\infty} dt \, t^{z-1} e^{-t}$ was used. With $z \, \Gamma[-z, a] = a^{-z} e^{-a} - \Gamma[-z + 1, a]$ and the fact that $A_3 \tau_s = A_5 \tau_s - 1$, we obtain after insertion of $X(t)$ into equation B.3,

$$V(t) = \exp\left[-\frac{t}{\tau_m^L} + \frac{\tau_s}{\Delta \tau_m^s} e^{-\frac{t}{\tau_s}} \right]$$

$$\times \left\{ E_L e^{-\frac{\tau_s}{\Delta \tau_m^s}} - E_s \left(e^{-\frac{\tau_s}{\Delta \tau_m^s}} - \exp\left[\frac{t}{\tau_m^L} - \frac{\tau_s}{\Delta \tau_m^s} e^{-\frac{t}{\tau_s}} \right] \right) \right.$$

$$+ \left(\Gamma\left[-\frac{\tau_s}{\tau_m^L}, \frac{\tau_s}{\tau_m^s} \right] - \Gamma\left[-\frac{\tau_s}{\tau_m^L}, \frac{\tau_s}{\Delta \tau_m^s} e^{-\frac{t}{\tau_s}} \right] \right)$$

$$\times \left(\frac{\tau_s}{\Delta \tau_m^s} \right)^{\frac{\tau_s}{\tau_m^L}} \frac{\tau_s}{\tau_m^L} (E_s - E_L) \right\}. \tag{B.4}$$

The latter can be further simplified by noting that

$$\Gamma\left[-\frac{\tau_s}{\tau_m^L}, \frac{\tau_s}{\Delta \tau_m^s} e^{-\frac{t}{\tau_s}} \right] = \Gamma\left[-\frac{\tau_s}{\tau_m^L}, \frac{\tau_s}{\Delta \tau_m^s} e^{-\frac{t}{\tau_s}}, \frac{\tau_s}{\Delta \tau_m^s} \right] + \Gamma\left[-\frac{\tau_s}{\tau_m^L}, \frac{\tau_s}{\Delta \tau_m^s} \right],$$

where $\Gamma[z, a, b] = \int_a^b dt \, t^{z-1} e^{-t}$ denotes the generalized incomplete gamma function. We obtain

$$V(t) = \exp\left[-\frac{t}{\tau_m^L} + \frac{\tau_s}{\Delta \tau_m^s} e^{-\frac{t}{\tau_s}} \right]$$

$$\times \left\{ E_L e^{-\frac{\tau_s}{\Delta \tau_m^s}} - E_s \left(e^{-\frac{\tau_s}{\Delta \tau_m^s}} - \exp\left[\frac{t}{\tau_m^L} - \frac{\tau_s}{\Delta \tau_m^s} e^{-\frac{t}{\tau_s}} \right] \right) \right.$$

$$\left. - \Gamma\left[-\frac{\tau_s}{\tau_m^L}, \frac{\tau_s}{\Delta \tau_m^s} e^{-\frac{t}{\tau_s}}, \frac{\tau_s}{\Delta \tau_m^s} \right] \left(\frac{\tau_s}{\Delta \tau_m^s} \right)^{\frac{\tau_s}{\tau_m^L}} \frac{\tau_s}{\tau_m^L} (E_s - E_L) \right\} \tag{B.5}$$

as the general form of the membrane potential (i.e., postsynaptic potential) time course following a single synaptic stimulation described by an exponential conductance time course.

B.2 Analytic Approximation of the PSP Peak Height. Equation B.5 provides a rather complicated expression for the PSP time course and is, therefore unsuitable for directly deducing a simple equation for the PSP peak amplitude we are looking for. However, guided by the general shape of the PSP, we will approximate equation B.5 using an α-function,

$$V_\alpha(t) = V_{\alpha 0} \frac{t}{\tau_\alpha} e^{-\frac{t}{\tau_\alpha}} + E_L, \tag{B.6}$$

where $V_{\alpha 0}$ denotes the maximum and τ_α the time constant of the α-function. The desired peak amplitude is then given by $V_{\max} = V_{\alpha 0} e^{-1}$.

In order to approximate $V(t)$, equation B.5, with $V_\alpha(t)$, we power-expand the difference $V(t) - V_\alpha(t)$ up to second order in t at $t = 0$. This yields the equations

$$0 = (E_L - E_s)\,\tau_\alpha + \Delta\tau_m^s V_{\alpha 0}\,,$$

$$0 = (E_L - E_s)\,\tau_\alpha^2 \left(\Delta\tau_m^s \tau_s + \tau_m^L \left(\Delta\tau_m^s + \tau_s\right)\right) + 2\tau_m^L \left(\Delta\tau_m^s\right)^2 \tau_s V_{\alpha 0},$$

from which the parameters $V_{\alpha 0}$ and τ_α can be deduced. We obtain

$$V_{\alpha 0} = \frac{2(E_s - E_L)\tau_m^L \tau_s}{\Delta\tau_m^s \tau_s + \tau_m^L \left(\Delta\tau_m^s + \tau_s\right)}, \tag{B.7}$$

which yields for the PSP peak amplitude

$$V_{\max} = \frac{2e^{-1}(E_s - E_L)\,\tau_m^L \tau_s}{\Delta\tau_m^s \tau_s + \tau_m^L \left(\Delta\tau_m^s + \tau_s\right)}. \tag{B.8}$$

In equation B.8, $\Delta\tau_m^s$ denotes the change in the membrane time constant at arrival of a synaptic input, and τ_m^L is the membrane time constant before the arrival of the synaptic input, which, due to the chosen baseline (membrane at rest for $t < 0$), equals the passive (leak) membrane time constant. However, in the general situation, τ_m^L has to be replaced by the total membrane time constant $\tau_m(t)$ at time t_0 of the arrival of a new synaptic event, which contains leak as well as synaptic contributions.

To optimize the applicability of equation B.8 in event-driven simulation strategies, we consider the relative change of the PSP peak amplitude as a function of the actual state with respect to a control state. Let $\tilde{V}_{\max}$ denote the PSP peak amplitude in the control state (e.g., the resting state) characterized by the total membrane time constants $\tilde{\tau}_m$. Then equation B.8 yields

$$V_{\max}(t) = \tilde{V}_{\max} \left(\frac{1}{\tilde{\tau}_m} + \frac{1}{\tau_s} + \frac{1}{\Delta\tau_m^s}\right) \left(\frac{1}{\tau_m(t)} + \frac{1}{\tau_s} + \frac{1}{\Delta\tau_m^s}\right)^{-1} \tag{B.9}$$

for the PSP peak amplitude following a synaptic input in the actual state at time t characterized by a total membrane time constant $\tau_m(t)$.

B.3 Incorporation of the Synaptic Reversal Potential. Equation B.5 shows that the full solution for the PSP depends not only on the average membrane conductance (see the previous section), but also on the actual membrane state $V(t)$ and, hence, the distance to the corresponding synaptic reversal potential E_s. Moreover, in the presence of synaptic reversal potentials, for example, for excitation and inhibition, the membrane will have an effective reversal state to which it decays exponentially with a time constant associated with the total membrane conductance. This effective reversal state is determined by the synaptic conductance contributions and the leak conductance, as well as the "distance" of the current membrane state to the respective reversal potentials of the conductances and leak.

To incorporate both effects in a simple approximation of the PSP peak amplitude, this way extending the result in equation B.9, we start from the membrane equation B.1. In the case of a single synaptic input, it can be rewritten in the form

$$\frac{dV(t)}{dt} + \frac{1}{\tau_m(t)}\left(V(t) - V_{rest}(t)\right) = 0, \tag{B.10}$$

where

$$V_{rest}(t) = \left(\frac{E_L}{\tau_m^L} + \frac{E_s}{\tau_m^s(t)}\right)\left(\frac{1}{\tau_m^L} + \frac{1}{\tau_m^s(t)}\right)^{-1}, \tag{B.11}$$

$$\frac{1}{\tau_m(t)} = \frac{1}{\tau_m^L} + \frac{1}{\tau_m^s(t)}, \tag{B.12}$$

$$\frac{1}{\tau_m^s(t)} = \frac{1}{\tau_m^s(t_0)}\,e^{-\frac{t-t_0}{\tau_s}} \qquad \text{for } t \geq t_0. \tag{B.13}$$

Due to the time dependence of $V_{rest}(t)$, equation B.10 does not provide a closed-form solution (see equation B.5) simple enough to build a basis for an IF neuron model usable within an event-bases simulation approach. In order to obtain such a form, we use the fact that a single synaptic input has only a minimal contribution to the total membrane time constant. Therefore, we can truncate the explicit time dependence of $V_{rest}(t)$ by replacing the synaptic contribution to the membrane time constant, $\tau_m^s(t)$ with its value at time t_0, that is, at the arrival of the synaptic event. Equation B.11 then yields

$$V_{rest}(t) \sim V_{rest} = \left(\frac{E_L}{\tau_m^L} + \frac{E_s}{\tau_m^s(t_0)}\right)\left(\frac{1}{\tau_m^L} + \frac{1}{\tau_m^s(t_0)}\right)^{-1}. \tag{B.14}$$

Note that V_{rest} will still indirectly depend on time, because $\tau_m^s(t_0)$ is updated whenever a synaptic event arrives.

To make the impact of synaptic reversal potentials on the PSP peak amplitude explicit, we extend the membrane equation B.1 by a constant stimulating current I_0:

$$\frac{dV(t)}{dt} = -\frac{1}{\tau_m^L}\left(V(t) - E_L\right) - \frac{1}{C}\,G_s(t)\left(V(t) - E_s\right) + \frac{1}{C}\,I_0\,. \tag{B.15}$$

Different values of I_0 will hold the membrane potential at different base values, from which we will deduce the desired dependence of the PSP peak height. Defining $E_L' = E_L + \frac{\tau_m^L}{C}\,I_0$ as the effective leak reversal in the presence of a constant current, equation B.15 can be brought into a form

$$\frac{dV(t)}{dt} = -\frac{1}{\tau_m^L}\left(V(t) - E_L'\right) - \frac{1}{C}\,G_s(t)\left(V(t) - E_s\right), \tag{B.16}$$

which has the same functional form as the original membrane equation B.1. Therefore, and because I_0 is assumed to be constant, we can proceed along the lines outlined in sections B.1 and B.2 and obtain for the PSP peak amplitude

$$V_{\max} = \frac{2e^{-1}(E_s - E_L')\,\tau_m^L\,\tau_s}{\Delta\tau_m^s\,\tau_s + \tau_m^L(\Delta\tau_m^s + \tau_s)}. \tag{B.17}$$

Note that E_L' denotes the base potential over which the PSP arises and therefore corresponds to the actual state of the membrane at the time of the synaptic input.

Finally, we deduce the relative change of the PSP peak amplitude with respect to a control state as a function of the actual state of the membrane. Let the actual state be characterized by the membrane time constant $\tau_m(t)$ and the membrane state variable $V(t)$. Let $\tilde{V}_{\max}$ denote the PSP peak amplitude in the control state (e.g., the resting state) characterized by the time constant $\tilde{\tau}_m$ and state variable $\tilde{V}$. Then we obtain for the PSP peak amplitude in the actual state

$$V_{\max}(t) = \tilde{V}_{\max}\,\frac{V(t) - E_s}{\tilde{V} - E_s}\left(\frac{1}{\tilde{\tau}_m} + \frac{1}{\tau_s} + \frac{1}{\Delta\tau_m^s}\right)\left(\frac{1}{\tau_m(t)} + \frac{1}{\tau_s} + \frac{1}{\Delta\tau_m^s}\right)^{-1}. \tag{B.18}$$

The first factor $(V(t) - E_s)/(\tilde{V} - E_s)$ is responsible for the effect of the distance of the actual membrane state to the reversal potential, whereas the

second term describes the scaling of the PSP peak amplitude as a function of the membrane time constant in accordance with equation B.9.

Appendix C: Extension to Nonlinear IF Neuron Models

In this appendix, we briefly present first attempts to generalize the idea behind the gIF models to neuronal models that contain, in addition to synaptic conductances, state-dependent currents due to active membrane conductances used, for example, to describe spike generation. We begin by analytically approximating the time course of a passive membrane after synaptic input in order to incorporate a more realistic PSP shape into the model (see section C.1). State equations for the quadratic integrate-and-fire (QIF, section C.2) and exponential integrate-and-fire (EIF, section C.3) neuronal models with conductance-based synaptic interactions will be presented. A complete description of this work as well as a detailed evaluation of the behavior of these models will be presented in a forthcoming study.

C.1 gIF Models with Realistic PSP Time Course. In appendix B.1, we simplified the exact solution (see equation B.3) of the passive membrane equation with exponential synaptic conductance time course (see equation B.1) in order to obtain an analytic expression for the PSP peak amplitude as a function of the actual membrane state and total membrane time constant (see sections B.2 and B.3). The advantage of this approach was that the deduced simple expression for the PSP peak amplitude allowed its use in the gIF neuron models as an instantaneous update value of the membrane state upon the arrival of a synaptic input. However, the temporal shapes of EPSPs and IPSPs are neglected, which might have a subtle impact on the cellular response characteristics, in particular its temporal aspects. Here, we analytically approximate the full solution and provide a simple expression for the PSP shape that can be used in event-driven simulation strategies.

Equation B.3 can be rewritten as

$$V(t) = e^{Q_1(t)} \left\{ E_L e^{-\frac{\tau_s}{\Delta \tau_m^s}} + \int_0^t ds\, e^{Q_2(s)} \left\{ \frac{E_s}{\Delta \tau_m^s} + \frac{E_L}{\tau_m^L} e^{\frac{s}{\tau_s}} \right\} \right\} \qquad (C.1)$$

with

$$Q_1(t) = -\frac{t}{\tau_m^L} + \frac{\tau_s}{\Delta \tau_m^s} e^{-\frac{t}{\tau_s}},$$

$$Q_2(t) = \frac{t}{\tau_m^L} - \frac{t}{\tau_s} - \frac{\tau_s}{\Delta \tau_m^s} e^{-\frac{s}{\tau_s}}.$$

Power-expanding $Q_1(t)$ and $Q_2(t)$ up to first order at $t = 0$ and using the boundary conditions $V(t) \longrightarrow E_L$ for $t \to 0$ and $t \to \infty$, equation C.1 can

be approximated by

$$V_{PSP}(t) = E_L + \frac{E_s}{\Delta\tau_m^s} \left(\frac{1}{\tau_s} - \frac{1}{\tau_m^L} - \frac{1}{\Delta\tau_m^s} \right)^{-1} \left\{ e^{-t\left(\frac{1}{\tau_m^L} + \frac{1}{\Delta\tau_m^s}\right)} - e^{-\frac{t}{\tau_s}} \right\}. \quad (C.2)$$

We note that this general form of the PSP time course as a difference between two exponentials was already suggested in the context of the spike response model (Jolivet & Gerstner, 2004) and quadratic integrate-and-fire models (Latham et al., 2000).

If the synaptic input arrives at time t_0 on top of a barrage with synaptic inputs, equation C.2 can be generalized to provide the desired expression of the PSP time course as a function of the actual membrane state $V(t_0)$ and membrane time constant $\tau_m(t_0)$. Following the argumentation presented in section B.3, we obtain for $t \geq t_0$

$$V_{PSP}(t) = E_L + \left(V(t_0) - E_L \right) e^{-(t-t_0)\left(\frac{1}{\tau_m(t_0)} + \frac{1}{\Delta\tau_m^s}\right)}$$

$$+ Q\, E_s \left(\frac{1}{\tau_m^s(t_0)} + \frac{1}{\Delta\tau_m^s} \right) \left(\frac{1}{\tau_s} - \frac{1}{\tau_m(t_0)} - \frac{1}{\Delta\tau_m^s} \right)^{-1}$$

$$\times \left\{ e^{-(t-t_0)\left(\frac{1}{\tau_m(t_0)} + \frac{1}{\Delta\tau_m^s}\right)} - e^{-\frac{t-t_0}{\tau_s}} \right\}, \quad (C.3)$$

where $\tau_m^s(t_0)$ denotes the synaptic contribution to the membrane time constant at time t_0 and $\Delta\tau_m^s$ the update of $\tau_m^s(t_0)$ due to the synaptic input (see equation 2.6). Q is a PSP scaling factor that was introduced in generalizing the approximation of equation C.1 to arbitrary effective reversal states. It primarily depends on the distance of the actual membrane state to the synaptic reversal potential, and a good approximation of Q is given by the first factor in equation B.18, thus yielding

$$V_{PSP}(t) = E_L + \left(V(t_0) - E_L \right) e^{-(t-t_0)\left(\frac{1}{\tau_m(t_0)} + \frac{1}{\Delta\tau_m^s}\right)}$$

$$+ \frac{E_s}{\Delta\tau_m^s} \frac{V(t_0) - E_s}{E_L - E_s} \left(\frac{1}{\tau_m^s(t_0)} + \frac{1}{\Delta\tau_m^s} \right) \left(\frac{1}{\tau_s} - \frac{1}{\tau_m(t_0)} - \frac{1}{\Delta\tau_m^s} \right)^{-1}$$

$$\times \left\{ e^{-(t-t_0)\left(\frac{1}{\tau_m(t_0)} + \frac{1}{\Delta\tau_m^s}\right)} - e^{-\frac{t-t_0}{\tau_s}} \right\}. \quad (C.4)$$

This defines, along with equations 2.6, 2.7, and 2.8 for updating the membrane time constant upon arrival of a synaptic input, the basis of a gIF4 model.

In order to evaluate the validity of the gIF4 model, we compared the EPSP and IPSP time course obtained from the analytic approximation,

equation C.4, with the numerical solution of the underlying passive membrane equation B.1 (LIFcd model). For both excitatory and inhibitory synaptic inputs, the gIF4 model described remarkably well the postsynaptic membrane potential time course (see Figure 12A) for all membrane potentials ranging from the leak reversal E_L up to the firing threshold E_{thres}. For the realistic synaptic and cellular parameter values used here, the deviation, or relative error, was smaller for leakier and, hence, faster membranes (see Figure 12B) and did not exceed 1% for times that covered the PSP peak (see Figure 12B, gray area). The latter suggests that an exact and computationally fast prediction of spike times based on the analytic form of the approximated EPSP time course given by equation C.4 should be possible. However, although an excellent agreement of the gIF4 model with the LIFcd model was reached for small or medium synaptic input rates (see Figure 12C), total input rates above 1 kHz led to deviations from the numerical simulation. The reason for this can be found in the approximative character of the PSP time course, in particular, the PSP peak amplitude scaling (factor Q in equation C.3). This error could be reduced by fine-tuning the quantal conductance of the synaptic input or the scaling factor Q. To what extent the observed deviations for high input rates compensate the simplicity and, thus, computational efficiency of the obtained analytic approximation remains to be investigated.

In contrast to the instantaneous update of the membrane state characteristic for the integrate-and-fire neuron models presented in section 2, the incorporation of a realistic PSP shape in the gIF4 model (equation C.4) no longer allows the application of the basic event-driven simulation strategy presented in section 4.1. Indeed, in models with instantaneous rise of the membrane potential, the firing threshold can be crossed only at the time of the synaptic input, whereas in models with EPSP time course, the membrane state can cross the threshold and thus generate an output spike even milliseconds after the synaptic input occurred. The latter makes the prediction of a future threshold crossing based on the EPSP time course necessary. In this case, a generalization of the event-driven simulation strategy (Hines & Carnevale, 2004) provides both an exact and computationally efficient way to simulate neural activity (see Figure 12D). First, upon arrival of a synaptic event at time t, the actual membrane state $V(t)$ is calculated from the membrane state $V(t_0)$ at the time t_0 of the previous synaptic input using equation C.4, and the membrane time constant $\tau_m(t)$ is updated using equations 2.7 and 2.8. Then equation C.4 is used to predict the time t_s of a possible future threshold crossing, which is emitted as an event into the network. If another synaptic input arrives before $t_1 < t_s$, the membrane potential is updated, and a possible new spike time t'_s will overwrite the previous prediction t_s. An implementation of this approach for the gIF4 model using the simple analytic form of the PSP time course, equation C.4, as well as evaluation of its precision and efficiency, will be the subject of a forthcoming study.

C.2 gQIF—A Conductance-Based Quadratic IF Model. In order to describe the effect of state-dependent currents due to active membrane conductances, we generalize the passive membrane equation B.1 by incorporating a nonlinear current $I_{act}(V(t))$,

$$\frac{dV(t)}{dt} = -\frac{1}{\tau_m^L}\left(V(t) - E_L\right) - \frac{1}{C}\,I_{act}(V(t)) - \frac{1}{C}\,I_{syn}(t)\,, \qquad (C.5)$$

where $I_{syn}(t)$ defines the synaptic current (e.g., Fourcaud-Trocmé et al., 2003). Depending on the functional form of $I_{act}(V(t))$, different models can be defined. In this and the following sections, we give the explicit form of the state equation for various models in the presence of synaptic conductance, thus defining the basis for nonlinear IF neuron models with presynaptic-activity dependent state dynamics. However, a detailed analytical and numerical investigation exceeds the framework of this article and will be the subject of a forthcoming study.

The quadratic integrate-and-fire (QIF) neuronal model is defined by (Latham et al., 2000; Feng, 2001; Hansel & Mato, 2001; Brunel & Latham, 2003; Fourcaud-Trocmé et al., 2003)

$$I_{act}(V(t)) = -\frac{C}{2\Delta_T\,\tau_m^L}\left(V(t) - E_T\right)^2 - \frac{C}{\tau_m^L}\left(V(t) - E_L\right) + I_T, \qquad (C.6)$$

where E_T, defined by

$$\left.\frac{dI_{act}(V)}{dV}\right|_{V=E_T} = -\frac{C}{\tau_m^L}, \qquad (C.7)$$

denotes the threshold membrane state at which the slope of the I–V curve vanishes,

$$I_T = \frac{C}{\tau_m^L}\left(E_T - E_L\right) + I_{act}(E_T) \qquad (C.8)$$

denotes the corresponding threshold current, and

$$\Delta_T = -C\left(\tau_m^L\,\left.\frac{d^2 I_{act}(V)}{dV^2}\right|_{V=E_T}\right)^{-1} \qquad (C.9)$$

the spike slope factor. If the synaptic input current exceeds the threshold current I_T, the membrane potential diverges in finite time to infinity. The latter can be used to define the discharge of a spike, after which the membrane potential is reset to a resting value.

If the synaptic current takes the form $I_{syn}(V(t)) = G_s^{\exp}(t)\left(V(t) - E_s\right)$ with synaptic conductance $G_s^{\exp}(t)$ given by equation B.2, we can define the basic

state equation for a QIF model with presynaptic-activity dependent state dynamics (gQIF model):

$$\frac{dV(t)}{dt} = \frac{1}{2\Delta_T\,\tau_m^L}\left(V(t) - E_T\right)^2 - \frac{1}{C}\,I_T - \frac{1}{\tau_m^s(t)}\left(V(t) - E_s\right) \qquad \text{(C.10)}$$

for $t \geq t_0$ with the time-dependent synaptic contribution to the membrane time constant $\tau_m^s(t)$ given by equation B.13. The latter is updated upon arrival of a synaptic event at time t_0 according to equation 2.7.

Unfortunately, equation C.10 is difficult to solve analytically due to the explicit time dependence of $\tau_m^s(t)$. However, if the conductance increment caused by a single synaptic input is small compared to the total membrane conductance (in the realistic cases considered here, the conductance change following a synaptic input is about 30 times smaller than the leak conductance; see Table 2), a good approximate solution of equation C.10 can be obtained by assuming a constant $\tau_m^s(t)$ between the arrival of two synaptic inputs at t_0 and t_1. When a new synaptic input arrives, $\tau_m^s(t_0)$ is updated according to equations 2.6 and 2.7. This approach was also used in the gIF3 model for the effective reversal state (equations 2.25 and B.14) and provided a good approximation even for low input rates. A detailed numerical analysis along with an analytical investigation of equation C.10 with respect to divergencies defining spiking events exceeds the framework of this article and will be the subject of a forthcoming study.

C.3 gEIF—A Conductance-Based Exponential IF Model. Along the lines outlined in the last section, an exponential integrate-and-fire (EIF) neuron model (Fourcaud-Trocmé et al., 2003) can be defined with

$$I_{act}(V(t)) = -\frac{C\,\Delta_T}{\tau_m^L}\,\mathrm{e}^{\frac{V(t)-E_T}{\Delta_T}}, \qquad \text{(C.11)}$$

where E_T and Δ_T are defined in equations C.7 and C.9, respectively. With a conductance-based synaptic current, we obtain the basic state equation for an EIF model with presynaptic-activity dependent state dynamics (gEIF model):

$$\frac{dV(t)}{dt} = -\frac{1}{\tau_m(t)}\left(V(t) - V_{rest}(t)\right) + \frac{\Delta_T}{\tau_m^L}\,\mathrm{e}^{\frac{V(t)-E_T}{\Delta_T}}, \qquad \text{(C.12)}$$

where the effective reversal state $V_{rest}(t)$ is given by equation B.11, and $\tau_m(t)$ obeys equations B.12 and B.13 with update $\Delta\tau_m^s$ upon arrival of a synaptic event (see equation 2.7) at time t_0. As in the case of the gQIF model, the state equation C.12 is not analytically solvable exactly. Again, for efficient use in event-driven simulation strategies, approximations remain the only tool to assess the membrane state at time t based on the state at the time

of the previous synaptic event t_0 and to predict possible threshold crossing for spike generation.

Acknowledgments

References

Abbott, L. F., & van Vreeswijk, C. (1993). Asynchronous states in networks of pulse-coupled oscillators. *Phys. Rev. E, 48*, 1483–1490.

Borg-Graham, L. J., Monier, C., & Frégnac, Y. (1998). Visual input evokes transient and strong shunting inhibition in visual cortical neurons. *Nature, 393*, 369–373.

Brumberg, J. C. (2002). Firing pattern modulation by oscillatory input in supragranular pyramidal neurons. *Neurosci., 114*, 239–246.

Brunel, N. (2000). Dynamics of sparsely connected networks of excitatory and inhibitory spiking neurons. *J. Comp. Neurosci., 8*, 183–208.

Brunel, N., Chance, F. S., Fourcaud, N., & Abbott, L. F. (2001). Effects of synaptic noise and filtering on the frequency response of spiking neurons. *Phys. Rev. Lett., 86*, 2186–2189.

Brunel, N., & Latham, P. E. (2003). Firing rate of the noisy quadratic integrate-and-fire neuron. *Neural Comput., 15*, 2281–2306.

Burns, B. D., & Webb, A. C. (1976). The spontaneous activity of neurons in the cat's visual cortex. *Proc. R. Soc. London B, 194*, 211–223.

Chance, F. S., Abbott, L. F., & Reyes, A. D. (2002). Gain modulation from background synaptic input. *Neuron, 15*, 773–782.

Christodoulou, C., & Bugmann, G. (2001). Coefficient of variation vs. mean interspike interval curves: What do they tell us about the brain? *Neurocomputing, 38–40*, 1141–1149.

Cragg, B. G. (1967). The density of synapses and neurones in the motor and visual areas of the cerebral cortex. *J. Anat., 101*, 639–654.

DeFelipe, J., Alonso-Nanclares, L., & Arellano, J. I. (2002). Microstructure of the neocortex: Comparative aspects. *J. Neurocytol., 31*, 299–316.

DeFelipe, J., & Fariñas, I. (1992). The pyramidal neuron of the cerebral cortex: Morphological and chemical characteristics of the synaptic inputs. *Prog. Neurobiol., 39*, 563–607.

Delorme, A., Gautrais, J., van Rullen, R., & Thorpe, S. (1999). SpikeNET: A simulator for modeling large networks of integrate and fire neurons. *Neurocomputing, 26–27*, 989–996.

Delorme, A., & Thorpe, S. J. (2003). SpikeNET: An event-driven simulation package for modeling large networks of spiking neurons. *Network: Comput. Neural Syst., 14*, 613–627.

Destexhe, A., Mainen, Z. F., & Sejnowski, T. J. (1994). Synthesis of models for excitable membranes, synaptic transmission and neuromodulation using a common kinetic formalism. *J. Comput. Neurosci., 1*, 195–230.

Destexhe, A., Mainen, Z., & Sejnowski, T. J. (1998). Kinetic models of synaptic transmission. In C. Koch & I. Segev (Eds.), *Methods of neuronal modeling* (pp. 1–26), Cambridge, MA: MIT Press.

Destexhe, A., & Rudolph, M. (2004). Extracting information from the power spectrum of synaptic noise. *J. Comput. Neurosci., 17*, 327–345.

Destexhe, A., Rudolph, M., Fellous, J.-M., & Sejnowski, T. J. (2001). Fluctuating synaptic conductances recreate in vivo–like activity in neocortical neurons. *Neurosci., 107*, 13–24.

Destexhe, A., Rudolph, M., & Paré, D. (2003). The high-conductance state of neocortical neurons in vivo. *Nature Rev. Neurosci., 4*, 739–751.

Evarts, E. V. (1964). Temporal patterns of discharge of pyramidal tract neurons during sleep and waking in the monkey. *J. Neurophysiol., 27*, 152–171.

Fellous, J.-M., Rudolph, M., Destexhe, A., & Sejnowski, T. J. (2003). Synaptic background noise controls the input/output characteristics of single cells in an in vitro model of in vivo activity. *Neurosci., 122*, 811–829.

Feng, J. (2001). Is the integrate-and-fire model good enough? A review. *Neural Netw., 14*, 955–975.

Fourcaud-Trocmé, N., Hansel, D., van Vreeswijk, C., & Brunel, N. (2003). How spike generation mechanisms determine the neuronal response to fluctuating inputs. *J. Neurosci., 23*, 11628–11640.

Froemke, R., & Dan, Y. (2002). Spike-timing-dependent synaptic modification induced by natural spike trains. *Nature, 416*, 433–438.

Gerstner, W., & Kistler, W. M. (2002). *Spiking neuron models* Cambridge: Cambridge University Press.

Gerstner, W., Ritz, R., & van Hemmen, J. L. (1993). A biologically motivated and analytically soluble model of collective oscillations in the cortex: I. Theory of weak locking. *Biol. Cybern., 68*, 363–374.

Gerstner, W., & van Hemmen, J. L. (1992). Associative memory in a network of "spiking" neurons. *Network, 3*, 139–164.

Gerstner, W., & van Hemmen, J. L. (1993). Coherence and incoherence in a globally coupled ensemble of pulse-emitting Units. *Phys. Rev. Lett., 71*, 312–315.

Giugliano, M. (2000). Synthesis of generalized algorithms for the fast computation of synaptic conductances with Markov kinetic models in large network simulations. *Neural Comput., 12*, 903–931.

Giugliano, M., Bove, M., & Grattarola, M. (1999). Activity-driven computational strategies of a dynamically regulated integrate-and-fire model neuron. *J. Comput. Neurosci., 7*, 247–254.

Gruner, J. E., Hirsch, J. C., & Sotelo, C. (1974). Ultrastructural features of the isolated suprasylvian gyrus in the cat. *J. Comp. Neurol., 154*, 1–27.

Gutkin, B. S., Ermentrout, G. B., & Rudolph, M. (2003). Spike generating dynamics and the conditions for spike-time precision in cortical neurons. *J. Comput. Neurosci., 15*, 91–103.

Hansel, D., & Mato, G. (2001). Existence and stability of persistent states in large neuronal networks. *Phys. Rev. Lett., 86*, 4175–4178.

Hansel, D., Mato, G., Meurier, C., & Neltner, L. (1998). On numerical simulations of integrate-and-fire neural networks. *Neural Comput., 10*, 467–483.

Hill, S., & Tononi, G. (2005). Modeling sleep and wakefulness in the thalamocortical system. *J. Neurophysiol., 93* 1671–1698.

Hines, M. L., & Carnevale, N. T. (1997). The NEURON simulation environment. *Neural Comput., 9*, 1179–1209.

Hines, M. L., & Carnevale, N. T. (2004). Discrete event simulation in the NEURON environment. *Neurocomputing, 58–60*, 1117–1122.

Hirsch, J. A., Alonso, J. M., Reid, R. C., & Martinez, L. M. (1998). Synaptic integration in striate cortical simple cells. *J. Neurosci., 18*, 9517–9528.

Hodgkin, A. L., & Huxley, A. F. (1952). A quantitative description of membrane current and its application to conduction and excitation in nerve. *J. Physiol., 117*, 500–544.

Holmes, W. R., & Woody, C. D. (1989). Effects of uniform and non-uniform synaptic "activation-distributions" on the cable properties of modeled cortical pyramidal neurons. *Brain Res., 505*, 12–22.

Hubel, D. (1959). Single-unit activity in striate cortex of unrestrained cats. *J. Physiol., 147*, 226–238.

Huguenard, J. R., Hamill, O. P., & Prince, D. A. (1988). Developmental changes in Na^+ conductances in rat neocortical neurons: Appearance of a slow inactivating component. *J. Neurophysiol., 59*, 778–795.

Izhikevich, E. M. (2001). Resonate-and-fire neurons. *Neural Netw., 14*, 883–894.

Izhikevich, E. M. (2003). Simple model of spiking neurons. *IEEE Trans. Neural Networks, 14*, 1569–1572.

Jolivet, R., & Gerstner, W. (2004). Predicting spike times of a detailed conductance-based neuron model driven by stochastic spike arrival. *J. Physiol. (Paris), 98*, 442–451.

Jolivet, R., Lewis, T. J., & Gerstner, W. (2004). Generalized integrate-and-fire models of neuronal activity approximate spike trains of a detailed model to a high degree of accuracy. *J. Neurophysiol., 92*, 959–976.

Knight, B. W. (1972). Dynamics of encoding in a population of neurons. *J. Gen. Physiol., 59* 734–766.

Koch, C. (1999). *Biophysics of computation*. New York: Oxford University Press.

Kuhn, A., Aertsen, A., & Rotter, S. (2004). Neuronal integration of synaptic input in the fluctuation-driven regime. *J. Neurosci., 24*, 2345–2356.

Lánský, P., & Rospars, J. P. (1995). Ornstein-Uhlenbeck model neuron revisited. *Biol. Cybern., 72*, 397–406.

Lapicque, L. (1907). Recherches quantitatives sur l'excitation électrique des nerfs traitée comme une polarization. *J. Physiol. Pathol. Gen., 9*, 620–635.

Latham, P. E., Richmond, B. J., Nelson, P. G., & Nirenberg, S. (2000). Intrinsic dynamics in neuronal networks. I. Theory. *J. Neurophysiol., 83*, 808–827.

LeMasson, G., Marder, E., & Abbott, L. F. (1993). Activity-dependent regulation of conductances in model neurons. *Science, 259*, 1915–1917.

Lytton, W. W. (1996). Optimizing synaptic conductance calculation for network simulations. *Neural Comput., 8*, 501–509.

Lytton, W. W., & Hines, M. L. (2005). Independent variable time-step integration of individual neurons for network simulations. *Neural Comput., 17*, 903–921.

Lytton, W. W., & Stewart, M. (in press). RBF: Rule-based firing for network simulations. *Neurocomputing*.

Markram, H., Wang, Y., & Tsodyks, M. (1998). Differential signaling via the same axon of neocortical pyramidal neurons. *Proc. Natl. Acad. Sci. USA, 95*, 5323–5328.

Matsumura, M., Cope, T., & Fetz, E. E. (1988). Sustained excitatory synaptic input to motor cortex neurons in awake animals revealed by intracellular recording of membrane potentials. *Exp. Brain Res., 70*, 463–469.

Mattia, M., & Del Giudice, P. (2000). Efficient event-driven simulation of large networks of spiking neurons and dynamical synapses. *Neural Comput., 12*, 2305–2329.

Mauro, A., Conti, F., Dodge, F., & Schor, R. (1970). Subthreshold behavior and phenomenological impedance of the squid giant axon. *J. General Physiol., 55*, 497–523.

Mehring, C., Hehl, U., Kubo, M., Diesmann, M., & Aertsen, A. (2003). Activity dynamics and propagation of synchronous spiking in locally connected random networks. *Biol. Cybern., 88*, 395–408.

Mountcastle, V. B. (1997). The columnar organization of the neocortex. *Brain, 120*, 701–722.

Nicoll, A., Larkman, A., & Blakemore, C. (1993). Modulation of EPSP shape and efficacy by intrinsic membrane conductances in rat neocortical pyramidal neurons in vitro. *J. Physiol., 468*, 693–710.

Noda, H., & Adey, R. (1970). Firing variability in cat association cortex during sleep and wakefulness. *Brain Res., 18*, 513–526.

Paré, D., Shink, E., Gaudreau, H., Destexhe, A., & Lang, E. J. (1998). Impact of spontaneous synaptic activity on the resting properties of cat neocortical neurons in vivo. *J. Neurophysiol., 79*, 1450–1460.

Prescott, S. A., & De Koninck, Y. (2003). Gain control of firing rate by shunting inhibition: Roles of synaptic noise and dendritic saturation. *Proc. Natl. Acad. Sci. USA, 100*, 2076–2081.

Rall, W. (1967). Distinguishing theoretical synaptic potentials computed for different somadendritic distributions of synaptic inputs. *J. Neurophysiol., 30*, 1138–1168.

Rauch, A., La Camera, G., Lüscher, H.-R., Senn, W., & Fusi, S. (2003). Neocortical pyramidal cells respond as integrate-and-fire neurons to in vivo like input currents. *J. Neurophysiol., 90*, 1598–1612.

Reutimann, J., Giugliano, M., & Fusi, S. (2003). Event-driven simulations of spiking neurons with stochastic dynamics. *Neural Comput., 15*, 811–830.

Ricciardi, L. M., & Sacerdote, L. (1979). The Ornstein-Uhlenbeck process as a model for neuronal activity. I. Mean and variance of the firing time. *Biol. Cybern., 35*, 1–9.

Rudolph, M., & Destexhe, A. (2001). Correlation detection and resonance in neural systems with distributed noise sources. *Phys. Rev. Lett., 86*, 3662–3665.

Rudolph, M., & Destexhe, A. (2003). The discharge variability of neocortical neurons during high-conductance states. *Neurosci., 119*, 855–873.

Rudolph, M., & Destexhe, A. (2005). Multi-channel shot noise and characterization of cortical network activity. *Neurocomputing, 65–66*, 641–646.

Senn, W., Markram, H., & Tsodyks, M. (2000). An algorithm for modifying neurotransmitter release probability based on pre- and postsynaptic spike timing. *Neural Comput., 13*, 35–67.

Shelley, M., McLaughlin, D., Shapley, R., & Wielaard, J. (2002). States of high conductance in a large-scale model of the visual cortex. *J. Comput. Neurosci., 13*, 93–109.

Shelley, M. J., & Tao, L. (2001). Efficient and accurate time-stepping schemes for integrate-and-fire neuronal networks. *J. Comput. Neurosci., 11*, 111–119.

Shu, Y., Hasenstaub, A., Badoual, M., Bal, T., & McCormick, D. A. (2003). Barrages of synaptic activity control the gain and sensitivity of cortical neurons. *J. Neurosci., 23*, 10388–10401.

Smith, D. R., & Smith, G. K. (1965). A statistical analysis of the continuous activity of single cortical neurons in the cat unanesthetized isolated forebrain. *Biophys. J., 5*, 47–74.

Softky, W. R., & Koch, C. (1993). The highly irregular firing of cortical cells is inconsistent with temporal integration of random EPSPs. *J. Neurosci., 13*, 334–350.

Song, S., & Abbott, L. F. (2001). Cortical development and remapping through spike timing–dependent plasticity. *Neuron, 32*, 339–350.

Steriade, M. (1978). Cortical long-axoned cells and putative interneurons during the sleep-waking cycle. *Behav. Brain Sci., 3*, 465–514.

Steriade, M., & McCarley, R. W. (1990). *Brainstem control of wakefulness and sleep.* New York: Plenum.

Steriade, M., Timofeev, I., & Grenier, F. (2001). Natural waking and sleep states: a view from inside neocortical neurons. *J. Neurophysiol., 85*, 1969–1985.

Stevens, C. F., & Zador, A. M. (1998a). Novel integrate-and-fire-like model of repetitive firing in cortical neurons. *In Proc. of the 5th Joint Symposium on Neural Comput.* (Vol. 8, pp. 172–177). La Jolla, CA: University of California, San Diego.

Stevens, C. F., & Zador, A. M. (1998b). Input synchrony and the irregular firing of cortical neurons. *Nature Neurosci., 1*, 210–217.

Stuart, G., & Spruston, N. (1998). Determinants of voltage attenuation in neocortical pyramidal neuron dendrites. *J. Neurosci., 18*, 3501–3510.

Svirskis, G., & Rinzel, J. (2000). Influence of temporal correlation of synaptic input on the rate and variability of firing in neurons. *Biophys. J., 79*, 629–637.

Szentagothai, J. (1965). The use of degeneration in the investigation of short neuronal connections. In M. Singer & J. P. Shade (Eds.), *Progress in brain research, 14* (pp. 1–32). Amsterdam: Elsevier.

Traub, R. D., & Miles, R. (1991). *Neuronal networks of the hippocampus.* Cambridge: Cambridge University Press.

Tsodyks, M., Mit'kov, I., & Sompolinsky, H. (1993). Pattern of synchrony in inhomogeneous networks of oscillators with pulse interaction. *Phys. Rev. Lett., 71*, 1280.

Watts, L. (1994). Event-driven simulations of networks of spiking neurons. In J. D. Cowan, G. Tesauro, & J. Alspector (Eds.), *Advances in neural information processing systems, 6* (pp. 927–934), San Mateo, CA: Morgan Kaufmann.

Wehmeier, U., Dong, D., Koch, C., & van Essen, D. (1989). Modeling the mammalian visual system. In C. Koch & I. Seger (Eds.), *Methods in neuronal modeling* (pp. 335–359). Cambridge, MA: MIT Press.

Wielaard, D. J., Shelley, M., McLaughlin, D., & Shapley, R. (2001). How simple cells are made in a nonlinear network model of the visual cortex *J. Neurosci., 21*, 5203–5211.